Structure and dynamics of a muti-domain nitric oxide synthase regulated by a C2 domain

Dhruva Nair and Brian R. Crane*

AUTHOR ADDRESS:
Weill Institute for Cell and Molecular Biology
Department of Chemistry and Chemical Biology
Cornell University, Ithaca, NY 14853, USA.

*For correspondence: bc69@cornell.edu

Short Title: syNOS is a C2-domain-regulated multidomain NOS.

Abstract

Nitric oxide synthase (NOS) is a widely studied multidomain redox enzyme that produces the key signaling molecule and cytotoxic agent nitric oxide (NO) for functions that range from mammalian vasodilation to prokaryotic antibiotic resistance. NOS enzymes from metazoans and cyanobacteria rely on dynamic associations of their oxygenase and coupled di-flavin reductase domains that have largely evaded detailed structural characterization. CryoEM studies of a representative dimeric six-domain Synechococcus NOS reveal the architecture of the full-length enzyme, which contains an unusual regulatory C2 domain, and additional nitric oxide deoxygenase (NOD) and pseudo-globin modules. Five distinct structural states depict how pterin binding couples to tight and loose oxygenase conformations and how the Ca^{2+}-sensitive C2 domain moves over 85 Å to alternatively regulate either the NOS or NOD heme center. The extended C-terminal tail and its dynamic interactions highlight an added layer of regulation required by multidomain NOSs compared to other di-flavin reductases.

Teaser: syNOS is a highly dynamic multi-domain oxidoreductase that harnesses a Ca^{2+}-sensitive C2 domain to modulate activity.

38

39

40 **Introduction**

41 Nitric oxide (NO) is a potent free-radical signal and cytotoxic agent found throughout biology (*1–*
42 *8*). Nitric Oxide Synthases (NOS) are homodimeric P450-like enzymes that produce NO through
43 the 5-electron oxidation of L-arginine (L-arg) to L-citrulline (*9–12*). NOSs comprise a heme-
44 containing oxygenase domain (NOS_{Oxy}) that is reductively activated by either an appended
45 reductase domain (NOS_{Red}, characteristic of metazoans) or an auxiliary reductase partner
46 (characteristic of prokaryotes) (Fig 1A) (*10–12*).

47 Mammalian NOSs (mNOSs) are multidomain enzymes composed of an N-terminal NOS_{Oxy} and a
48 C-terminal NADPH-dependent NOS_{Red}, bridged by a calmodulin (CAM)-binding domain (NOS_{CBD};
49 Fig. 1A). NOS_{Red} belongs to the cytochrome P450 reductase (CYPOR) family and as such, is
50 further divided into a NOS_{Oxy}-proximal FMN-binding flavodoxin domain (NOS_{Fld}) and an FAD-
51 and NADPH-binding ferredoxin-$NADP^+$ reductase module (NOS_{FNR}) (*10–13*). NOS_{Oxy} utilizes
52 tetrahydrobiopterin (BH_4) or tetrahydrofolate for rapid heme reduction during oxygen activation
53 (*14*). To reduce heme for oxygen binding, electrons flow from NADPH -> FAD -> FMN(H)• ->
54 Heme-Fe^{3+}. Ca^{2+}- CAM enhances heme reduction by facilitating the traverse of NOS_{Fld} ~70 Å
55 from a shielded position in a conformationally locked state of NOS_{Red} to a productive binding
56 interaction with NOS_{Oxy} (*15–18*).

57 Given their medicinal importance (*19*), NOSs have been extensively studied in mammals, which
58 have three isoforms: 1) endothelial NOS (eNOS, regulation of the vasculature), 2) neuronal NOS
59 (nNOS, regulation of neuronal function), and 3) inducible NOS (iNOS, immune responses to
60 pathogens and cancer cells) (*11*, *20–22*). Most prokaryotic NOSs have fewer domains than their
61 metazoan counterparts and have diverse functions that include participation in stress
62 responses, antibiotic resistance and biosynthesis of secondary metabolites (*23–27*).

63 To mitigate NO cytotoxicity, prokaryotes oxidize NO to NO_3^- with flavohemoprotein (Hmp),
64 which combines a heme-reducing flavin reductase with an oxygen-activating globin domain. In

65 contrast, mammals oxidize NO with hemoglobin, cytoglobin and neuroglobin, which obtain
66 reduced equivalents from various environmental factors (*28–30*).

67 Cyanobacterial NOSs represent a bridge between metazoan and prokaryotic NOSs (*26*, *31–34*).
68 They comprise an mNOS architecture fused to an N-terminal globin domain, as exemplified by
69 the 1468-residue NOS from *Synechococcus sp*. PCC 7335 (i.e. syNOS, Fig. 1A). Like mNOS, Ca^{2+}
70 activates syNOS, despite syNOS lacking a CBD and Synechococcus lacking an obvious CAM
71 homolog (*34*). The syNOS globin domain (NOS_{Glb}) oxidizes NO to NO_3^- as a nitric oxide
72 dioxygenase (NOD) and, when considered with $syNOS_{FNR}$, resembles Hmp (*34*).

73 Ca^{2+}-CAM regulates mNOS activity by controlling the motions and associations of NOS_{Oxy} and
74 NOS_{Red} that allow electron transfer (ET) between them. Owing to the dynamic nature of
75 turnover and inactivated states of full-length NOSs, they have evaded characterization by direct
76 structural methods. Single particle electron microscopy (EM) in conjunction with chemical
77 crosslinking and hydrogen-deuterium exchange mass spectrometry (HDX-MS) have yielded
78 informative, if incomplete, structural information (*35–39*). These studies, along with
79 biochemical and spectroscopic characterization (*12*, *40–44*) have motivated a model of mNOS
80 conformational dynamics that involves three states: i) input, wherein NOS_{Fld} closely associates
81 with NOS_{FNR} so that the NOS_{Red} FAD can be reduced by NADPH; ii) intermediate, wherein NOS_{Fld}
82 transitions between its closed position next to NOS_{FNR} and an interaction with NOS_{Oxy}; and iii)
83 output, wherein Ca^{2+}-CAM promotes docking of NOS_{Fld} onto the NOS_{Oxy} of the adjacent subunit
84 (*44–47*). Although cryoEM has provided residue-level information on NOS_{Oxy}, NOS_{Red} positioning
85 has been challenging to discern owing to its conformational heterogeneity (*35*, *46*).

86 Herein, we resolve domain configurations of the multi-domain syNOS by cryoEM in conjunction
87 with further characterizing ET properties associated with its NOS and NOD activities. We
88 capture resting and dynamic states of the enzyme and identify an atypical C2-like domain that
89 acts as a reversible lynchpin to mediate Ca^{2+} sensitivity. An elaborated C-terminal tail (CTT) (*22*)
90 of NOS_{Red} , key for regulation of mNOS, maintains a conformationally locked dimer and
91 represents an expansion of the regulatory mechanisms seen within the di-flavin reductase
92 family.

Results and Discussion

SyNOS expression, purification and crosslinking mass spectrometry

Full-length *Synechococcus PCC 7335* NOS (syNOS) was fused to an N-terminal-twin strep affinity tag and co-expressed along with *E. coli* HSP90 and GAPDH, in BL21(DE3) and purified through a series of affinity and size exclusion columns (SEC) (see Methods, Fig. S1) (*46*, *48*, *49*). As found previously (*34*), syNOS purified as a mixture of monomers and dimers. SEC fractions were tested for NO production with L-arg and NADPH and active fractions were applied to glow-discharged Cu-Quantifoil grids, vitrified and imaged on either a Talos Arctica or Titan Krios. Prior to freezing, samples were incubated with or without Ca^{2+}/L-arg/NADPH and excess BH_4 (Table S1).

To complement cryoEM and gain further insight into domain dynamics we subjected purified syNOS dimer fractions to disuccinimidyl dibutyric urea (DSBU) crosslinking mass spectrometry (XL-MS), under inactive (Ca^{2+}-depleted) and turnover conditions (see methods for assay conditions). Peptide coverage was relatively high for both (inactive state, 91%; and turnover state, 93%) but only a limited number of intra/intersubunit Lys-to-Lys crosslinks were identified (Table S2).

Structure determination of inactivated full-length syNOS

SyNOS data sets and the states within are summarized in Table S1 and described below. Two datasets of syNOS samples lacking Ca^{2+}, L-arg and NADPH were collected on a Talos Arctica equipped with a K3 detector. Dataset (DS) 1 (1215 micrographs) and DS2 (4055 micrographs) were initially preprocessed using CryoSPARC (Fig. S2 and S3), then subjected to particle picking using CRYOLO and finally refined in CryoSPARC (*50*, *51*). During 2D classification multiple classes emerged resembling a symmetric full-length dimer (syNOS-Sym). DS1 produced a syNOS-Sym overall resolution of 3.8 Å (47 K particles), and DS2 produced a NOS-Sym map of 4.7 Å resolution (84 K particles).

120 In addition, an asymmetric class (syNOS-Asym) became apparent in both DS1 and DS2 that
121 lacked density for one $syNOS_{Red}$ and one $syNOS_{C2}$. DS1 produced a syNOS-Asym map with the
122 nominal resolution of 3.67 Å (67 K particles), whereas DS2 yielded a 4.00 Å resolution map (265
123 K particles). In syNOS-Asym, uninterpretable electron density surrounds the position of the
124 vacated $syNOS_{Red}$ indicative of conformational disorder for this subunit.

125 3D-refinement of syNOS-Sym gave clear electron density for secondary structure, cofactors and
126 in many cases, residue side chains. Portions of each subunit were less well defined yet still
127 allowed unambiguous placement of the constituent domains. Inspection of the electron density
128 indicated that the homodimer interface was structurally heterogeneous. To better reconstruct
129 the full-length dimer, we combined the syNOS-Sym particle stacks from DS1 (47 K particles) and
130 DS2 (84 K particles) and re-refined the density alignment for 3D-variability (VA) and 3D-Flex
131 analysis. We explored C1, C2 and C2 (relaxed) symmetries which yielded 3.99 Å, 3.95 Å and 3.95
132 Å nominal resolutions, respectively, with the C2(relaxed) refinement chosen for further
133 flexibility analysis (Fig. S4, discussed below). The C2 symmetry-imposed electron density was
134 sufficient for model building and refinement (Table S3).

135

136 <u>Structure determination of turnover syNOS with Ca^{2+} and L-arginine</u>

137 DS3 (Fig. S5) (5019 micrographs) represented syNOS incubated with Ca^{2+}, additional BH_4 and L-
138 arg and was collected on a Titan Krios equipped with a K3 detector. Micrographs were initially
139 preprocessed using CryoSPARC (Fig. S5), then subjected to particle picking with CRYOLO and
140 finally refined in CryoSPARC. During 2D classification, multiple classes emerged resembling NOS-
141 Asym but also a state that lacked density for $syNOS_{Red}$ on both subunits. The latter state
142 resembles previously determined nNOS cryoEM structures that resolved a NOS_{Oxy} homodimer
143 but lacked density for NOS_{Red} owing to conformational disorder (*36*). We refer to this class as
144 the a "loose" turnover state ($NOS\text{-}TO_L$), because the $syNOS_{Oxy}$ interface is expanded relative to a
145 typical "tight" $mNOS_{Oxy}$ dimer. 2D classes of $NOS\text{-}TO_L$ gave density plumes at the interface
146 characteristic of poor signal alignment, indicative of a conformationally heterogeneous particle,
147 hence a composite map from two local refinements was created(PDB:9Q15). syNOS-Asym

148 (PDB:9Q0Y) was refined to a nominal resolution of 3.19 Å (71 K particles), whereas syNOS-TO_L
149 (PDB:9Q0X) was resolved to 3.6 Å resolution (61 K particles, Table S3).

150

151 DS4 was collected from the same conditions on the 200 KV Talos Arctica equipped with a K3
152 detector. These grids, which had thicker cubic ice, produced an intermediate resolution
153 turnover state with a tight $syNOS_{Oxy}$ dimer interface (syNOS-TO_T) that more closely resembles
154 crystal structures of BH_4-bound $mNOS_{Oxy}$ (Fig. S6). SPA is possible from cubic ice conditions,
155 which is known to favor contraction (shrinkage) of protein structure, although the mechanisms
156 for this behavior are largely unknown (*52*).

157

158 <u>Structure determination of monomeric syNOS in turnover conditions</u>

159 DS5 (9036 micrographs) of syNOS incubated with additional BH_4, Ca^{2+}, L-arg and NADPH was
160 collected on a Titan Krios equipped with a Falcon 3 detector (Fig. S7). For this dataset, the
161 homodimers appeared primarily dissociated into monomers (syNOS-Mon). Unlike syNOS-Asym,
162 in syNOS-Mon, even $syNOS_{Oxy}$ appeared as a monomer. The micrographs were processed
163 through CryoSPARC with multiple rounds of 3D particle stack cleaning to remove damaged
164 particles (Fig. S7). The syNOS-Mon (PDB:9Q05) density was refined to 3.09 Å resolution (45 K
165 particles), with discernible sidechains and cofactors, although neither Ca^{2+}, nor L-arg could be
166 identified in the map (Table S3).

167

168 <u>Full-length syNOS ($syNOS_{FL}$) molecular architecture</u>

169 In the absence of Ca^{2+}, the syNOS-Sym(PDB:9Q06) state of the full-length enzyme ($syNOS_{FL}$)
170 forms a compact C2-symmetric homodimer composed of six domains per subunit (Fig. 1B,C,D);
171 the domain arrangements divide the protein into two redox modules: i) an Fld-FNR module with
172 an N-terminal C2 domain (residues 1-134) bound at the Oxy-FNR interface and ii) a Glb-Oxy
173 module, that also contains an 8-helical pseudo-globin domain that does not bind heme

174 (syNOS$_{pGlb}$, residues 179-339). Three extended linkers connect the most mobile domains, with
175 L1 (44 residues) connecting syNOS$_{C2}$ to syNOS$_{pGlb}$, L2 (10 residues) connecting syNOS$_{Oxy}$ to
176 syNOS$_{Fld}$ and L3 (13 residues) connecting syNOS$_{Fld}$ to syNOS$_{FNR}$ (Fig. S8).

177 In this symmetric "locked" state, syNOS dimerizes through interactions of syNOS$_{Oxy}$ (residues
178 474-852), and syNOS$_{pGlb}$, which bridges the gap between syNOS$_{Glb}$ (residues 340-473) and
179 syNOS$_{Oxy}$ (Fig. 1B, C). SyNOS does not contain a β-hairpin region and tetrahedral zinc-binding
180 site formed at the mNOS$_{Oxy}$ dimer interface; instead syNOS$_{pGlb}$ occupies this position, although
181 an insertion between αD/ αE (residues 245-263), that would superimpose on the mNOS zinc-
182 binding site is not well defined by the electron density (Fig. S9 A, B, C). The syNOS$_{Oxy}$ C-terminal
183 helical hairpin acts as an interaction hub at the center of the subunit by contacting syNOS$_{Fld}$,
184 syNOS$_{FNR}$, syNOS$_{Glb}$ and the syNOS$_{C2}$ domain.

185 3D variable analysis (3DVA) and 3D Flexible refinement (3DFlex) conducted on syNOS-Sym (
186 PDB:9Q06), revealed that syNOS subunits "breathe" between tight, ordered associations that
187 bind BH_4 within the helical lariats and more separated looser associations with lower density for
188 these regions (Movie S1), not unlike the "tight" and "loose" dimer states previously observed
189 for *B. subtilis* NOS (*53–55*). Most structures, except for NOS-TO$_T$, lacked density for the helical
190 lariats and BH_4, which compose the center of the syNOS$_{Oxy}$ dimer interface (Fig. S9). XL-MS
191 indicated that syNOS in turnover conditions produced three additional interfacial crosslinks
192 between syNOS$_{pGlb}$ and syNOS$_{Oxy}$ compared to the inactive protien (Fig S10 A – B). Thus, the
193 active state favors a tighter dimer interface, consistent with BH_4 binding. Samples collected in
194 thicker ice favored this tight association (syNOS-TO$_T$). In addition to an ordered NOS$_{Oxy}$ interface
195 and density for BH_4, NOS-TO$_T$ displayed new contacts between L1 and αA (syNOS$_{pGlb}$) on one
196 subunit and α9 (syNOS$_{Oxy}$) on the opposing subunit. Hence, L1 may influence syNOS$_{pGlb}$
197 positioning, which in turn propagates structural stability to the dimer interface (Fig. S9B).

198 The previously unannotated and uncharacterized N-terminal domain (residues 1-134) takes the
199 form of a tightly packed 8-stranded β-sandwich, capped by peripheral loops at each end (Fig.
200 1C, D). This structure strongly resembles a C2 domain (syNOS$_{C2}$), which is usually associated
201 with Ca^{2+}-dependent membrane targeting in eukaryotes and typically not found in prokaryotes.

202 (*56*, *57*) $SyNOS_{C2}$ brackets the backside of the $syNOS_{Oxy}$ heme pocket and $syNOS_{FNR}$ (residues
203 1017-1468; Fig. 1C). In NOS-Sym, $syNOS_{FNR}$ latches onto $syNOS_{Glb}$ through the ordered CTT,
204 which also binds to $syNOS_{Fld}$ (residues 863-1003; Fig. 1B, C).

205 $SyNOS_{Fld}$ and $syNOS_{FNR}$ comprise a canonical NOS reductase unit in a closed conformation with
206 the FMN-FAD isoalloxazine cofactors aligned in a planar end-to-end configuration (Fig. 2). To
207 facilitate ET between subunits, mNOSs rearrange to position the NOS_{Fld} domain < 15 Å from the
208 NOS_{Oxy} heme on the opposing subunit (*58*). Residue conservation, cross-linking and HDX-MS
209 indicate that NOS_{Fld} interacts dynamically on the backside of the heme pocket at a conserved
210 Trp residue (356 in human eNOS) (*36–38*, *55*). $SyNOS_{C2}$ blocks this position and would have to
211 move to allow productive ET from $syNOS_{Fld}$, which also must displace from its shielded
212 interaction with $syNOS_{FNR}$ (*38*). Notably, syNOS lacks the mNOS CBD (~30 residues) that upon
213 CAM binding favors the ET competent 'output state' (Fig. 2A-C) (*17*, *38*, *59*, *60*). However, the
214 syNOS interdomain linkers also likely mediate domain motions. These linkers generally have
215 extended conformations, with the longest, L1, traversing ~60 Å. The threading of L1 beneath L2
216 implies that any C2 movement will displace L2 and thereby cause $syNOS_{Fld}$ to move "up-and-
217 over" toward the adjacent $syNOS_{Oxy}$ subunit (Fig. S8). In comparison to the interdomain
218 interactions implied by the 25 Å resolution nNOS + CAM structure by negative-stain EM (*37*),
219 $syNOS_{Fld}$ likely undergoes a different trajectory to interact with $syNOS_{Oxy}$ in part because
220 $syNOS_{Glb}$ will block the CAM-directed conformational change proposed for nNOS.

221

222 <u>$SyNOS_{Red}$ is distantly related, but structurally similar, to cytochrome P-450 reductase (CYPOR)</u>

223 $SyNOS_{Red}$, $mNOS_{Red}$, sulfite reductase diflavin reductase (SIRFP), and methionine synthase
224 reductase (MTRR) belong to the cytochrome P450 reductase (CYPOR) family of di-flavin
225 reductases (Fig. S11) (*61–64*). Di-flavin reductases perform three-separate ET reactions i)
226 hydride transfer from NADPH/NADH to the FNR FAD cofactor ii) sequential ET from the FNR to
227 the Fld iii) ET from the Fld to an electron acceptor. Activities (i) and (ii) occur when the di-flavin
228 reductase is trapped in a "closed" conformation permitting first hydride and then electron

229 transfer along the sequence NADPH->FAD->FMN(H)• with activity (iii) requiring an "open"
230 conformation that frees the Fld to reduce the acceptor (e.g. NOS_{Oxy} or cytochrome c).

231 Analysis by sequence clustering, phylogenetic estimation using maximum likelihood (PhyML)
232 and multiple structure alignments (MSTA) indicated that $syNOS_{Red}$ and $mNOS_{Red}$ are outgroups
233 relative to CYPORs (Fig. S11); yet, $syNOS_{Red}$ is more closely related in structure to CYPOR than to
234 $nNOS_{Red}$ or other di-flavin reductases (Fig. 2 and S11) (*22*). Nevertheless, key differences arise in
235 the structural and electrostatic features that stabilize the reductase closed conformation in
236 syNOS (NOS-Sym) compared to CYPOR (Fig. 2A-C). CYPORs and $mNOS_{Red}$ stabilize the closed
237 conformation by way of an interfacing-region 1 (IR1) between an acidic patch surrounding the
238 $CYPOR_{Fld}$ FMN cofactor and a complementary basic patch surrounding the $CYPOR_{FNR}$ FAD
239 cofactor (Fig. 2B,C). An additional IR2 associates the Fld internal helices to the FNR control
240 region. $SyNOS_{Red}$ lacks electrostatic complementarity within IR1 and residue complementary
241 within IR2. Instead, regions of the CTT (CTT-IR) and the C2 domain mediate interactions
242 between the Fld and FNR in the $syNOS_{Red}$ closed conformation (Fig. 3A).

243 The CTT, shared by $syNOS_{Red}$ and $mNOS_{Red}$, are important for redox flux in NOS but are not
244 found in canonical CYPORs (Fig. 2A-C) (*22*, *46*). These enzymes also share a β-finger (syNOS
245 residues 1100-1132) that resides closer to the Fld domain in $syNOS_{Red}$ (~7.5 Å) compared to
246 $mNOS_{Red}$ (~17 Å), thereby suggesting either a differing structural roles for this element or
247 revealing a conformational state that $nNOS_{Red}$ can also assume (Fig. 2C). $syNOS_{Red}$ also lacks the
248 $mNOS_{Red}$ Fld autoinhibitory regulatory loop (AI, nNOS residues 836-849) that destabilizes CAM
249 binding at low levels of Ca^{2+} (Fig 2B) (*61*, *65*). Although syNOS, $nNOS_{Red}$, and CYPOR stabilize
250 their closed conformations through different interactions, they all produce a coplanar
251 orientation and similar separation between the FAD and FMN cofactors (~13 Å from flavin N_5-to-
252 N_5).

253

254 <u>NOS CTTs are enzyme-specific conformational regulators of ET.</u>

255 CTTs, thought to be an mNOS addition within the conserved CYPOR family (*66*), are 20-30
256 residue helical extensions that auto-inhibit reduction of NOS_{Fld} by NOS_{FNR} (Fig. 3). Sequence

257 alignments show no discernable residue similarity between the syNOS CTT and CTTs of the
258 three mNOS isoforms or that of the most similar eukaryotic NOS sequence from the diatom *T.*
259 *minus* (Fig. S12). The lack of sequence similarity between $syNOS_{CTT}$ and $mNOS_{CTT}$, despite
260 substantial similarity in the preceding $syNOS_{FNR}$ domains, implies convergent evolution of these
261 CTTs, likely in concert with the addition of $syNOS_{Glb}$.

262 Unlike previous NOS_{Red} structures that capture only a portion of the CTT, the syNOS structure
263 resolves the entire CTT and its interactions with $syNOS_{FLd}$ and $syNOS_{Glb}$ (Fig. 3, S13A). Compared
264 to other NOSs, the 27-residue syNOS CTT divides into two perpendicular helices (CTT_1 and CTT_2;
265 residues 1440-1468; Fig. 3A). CTT_1 locks the position of $syNOS_{Fld}$ in the canonical Fld-FNR closed
266 conformation. CTT_1 (residues 1446-1458) interacts with the FMN ligating loops of NOS_{Fld}
267 (residues 984-989 and 951-960). In this interface, key residue contacts likely influence ET-
268 competent conformational states of $syNOS_{Fld}$ (Fig. 3C-D). CTT_1 Lys987 likely modulates Fld
269 dynamics by ordering residues that coordinate the FMN pyrophosphate groups. Indeed, the
270 Lys987Ala variant, which disrupts the Lys987/Glu1454 salt-bridge, has a much more extended,
271 flexible structure by small angle X-Ray scattering (SAXS) than does the WT (Fig. S14). The second
272 CTT helix (CTT_2, residues 1460-1468) is absent in other NOSs and CYPORs, likely because it binds
273 to the atypical $syNOS_{Glb}$ (Fig. 3A). Indeed, an aliphatic patch on CTT_2 interacts with the
274 hydrophobic crevice between residues 358-392 on $syNOS_{Glb}$ (Fig 3A-B). Specific salt-bridges and
275 hydrogen bonds among CTT_2, $syNOS_{Glb}$ and $syNOS_{Fld}$, help to stabilize the Ca^{2+}-free closed
276 conformation of syNOS (Fig. 3D,E). In turnover conditions, XL-MS revealed a loss of crosslinks
277 between the CTT and FNR, which underscores the role of the CTT in mediating dynamics of
278 $syNOS_{Red}$ (Fig S10C , Table S2).

279 $SyNOS_{Red}$ has distinct reactivity toward the surrogate electron acceptor cytochrome c (Cc),
280 compared to $mNOS_{Red}$ and other CYPOR family members. The CTT lowers Cc reduction by NOS_{Fld}
281 in both syNOS and nNOS, but the Ca^{2+} dependence is opposite. In the absence of Ca^{2+}, removal
282 of the CTT does not affect Cc reduction by syNOS (Fig. S15). Ca^{2+} decreases Cc reduction by
283 almost 4-fold, but removal of the CTT reactivates Cc reduction (Fig. S15). In mNOS, Ca^{2+}-CAM
284 increases, rather than decreases Cc reduction (*67*, *68*) and CTT removal increases activity
285 further. Furthermore, replacing the $mNOS_{FNR}$ domain with $CYPOR_{FNR}$, which lacks a CTT, switches

286 the Ca^{2+}-CAM dependence of mNOS such that Cc reduction now decreases ~4-fold with Ca^{2+}-
287 CAM (*67*, *68*), much like for syNOS + Ca^{2+}. These Cc reduction behaviors among NOS proteins
288 likely reflect differences in the relative strength of interactions among NOS_{Fld}, NOS_{FNR}, the CTT,
289 NOS_{Oxy} and Cc itself. Interestingly, syNOS structures in the Ca^{2+}-depleted states (NOS-Sym, NOS-
290 Asym, NOS-Mon) revealed a stable, closed Fld, whereas the Ca^{2+} turnover states (NOS-$TO_{1,2}$) had
291 a mobile undiscerned Fld domain, seemingly *more* conducive to Cc reduction, not less.
292 However, in the Ca^{2+}-state, the Fld domain may partition more frequently toward NOS_{Oxy}, which
293 would compete with Cc and thereby reduce Cc reduction rates. In mNOS, if the Fld-to-Oxy
294 interaction is weaker than in syNOS. relieving a stronger CTT-to-Fld interaction with Ca^{2+}-CAM
295 may favor the Fld-to-Cc interaction.

296

297 <u>The CTT-stablizied closed conformation of $syNOS_{Red}$ limits flavin reduction.</u>

298 $SyNOS_{FL}$ and $syNOS_{Red}$ rates of flavin reduction by NADPH, measured through anaerobic
299 stopped-flow experiments, were biphasic and resembled the flavin reduction kinetics of CYPOR
300 and $nNOS_{Red}$ bound to Ca^{2+}-CAM (Fig. S16A) (*69*). However, NADPH reduces $syNOS_{FL}$ at a ~74-
301 fold slower rate than $syNOS_{Red}$ implying that the closed conformation of $syNOS_{FL}$ restricts
302 hydride transfer from NADPH to FAD (Fig. S16B-D). The lower FAD reduction rate in $syNOS_{FL}$ is
303 surprising because $syNOS_{Red}$ lacks an NADP(H)-ligating Arg (1400 in rat nNOS) known to inhibit
304 electron flow in CAM-free nNOS/eNOS (*70*). In nNOS, the Arg1400Ser substitution increases
305 flavin reduction while decreasing NO synthesis (*70*). Because syNOS contains an Asn residue at
306 the 1400 position it would be predicted to have a faster flavin reduction rate than $nNOS_{Red}$
307 (*70*). However, the $syNOS_{Glb}$-to-CTT interaction, unique to syNOS, may especially stabilize
308 conserved CTT residue Trp1440 (*71*), which blocks the nicotinamide group of NADPH from
309 approaching the FAD isoalloxazine ring for hydride transfer (Fig. S16B). The CTT enforced rigidity
310 in syNOS (also reflected in the XL-MS data, Fig. S10C) may compensate for the modified $NADP^+$-
311 binding pocket that lacks an autoinhibitory Arg1400 equivalent. Notably, compared to nNOS and
312 CYPOR the nicotinamide moiety in syNOS-Mon adopts an atypical conformation that is

313 intermediate to the reduction incapable $NADP^+$ conformation seen in nNOS (PDB:1TLL) and the
314 $NADP^+$/FAD stacked conformation seen in the CYPOR W677X variants (PDB:1AJO, Fig. S16D).

315

316 <u>Ca^{2+} regulates syNOS activity through a C2-like domain</u>

317 The lack of a CAM-CBD interaction in syNOS renders its Ca^{2+}sensitivity enigmatic. However,
318 $syNOS_{C2}$ structurally resembles C2 domains that mediate membrane recruitment by binding
319 Ca^{2+} (Fig. 4) particularly; mouse perforin C2 (Fig. 4A) (*56*, *57*, *72*).

320 In the closed conformation, $syNOS_{C2}$ forms a tripartite interface with the $syNOS_{Oxy}$ domain and
321 the FNR control region (Fig. 4B). Two regions of salt-bridges mediate the C2-Oxy interface (Fig.
322 4B). In particular, the interaction between $syNOS_{C2}$ Arg107 and NOS_{Oxy} Glu568, positions the C2
323 domain beside Trp715, the proposed site of $mNOS_{Fld}$ binding onto $mNOS_{Oxy}$ (*38*). A basic patch
324 on the C2-domain and a complementary acidic patch on α-helix 1162-1173 of the FNR-control
325 domain wedges the C2 between $syNOS_{Oxy}$ and $syNOS_{Fld}$ (Fig. 4C). Because $syNOS_{C2}$ blocks the
326 putative Fld-Oxy contact; displacement of $syNOS_{C2}$ would decrease conformational restraints on
327 $syNOS_{Red}$ (particularly the L2 linker) and relieve steric hindrance on the backside of the heme
328 pocket.

329 A variant devoid of the C2 domain ($syNOS_{\Delta C2}$, residues 179-1468) has no NOS activity but retains
330 Cc-reduction activity (Fig. S14). Strikingly, $syNOS_{\Delta C2}$ has a high WT-like Cc-reduction rate that is
331 uninhibited by Ca^{2+}. In keeping with an enzyme unconstrained by inhibitory interactions. SAXS
332 data indicates that the global flexibility of $syNOS_{\Delta C2}$ exceeds that of the WT and the more
333 flexible K987A variant (Fig. S14). Thus, the C2 domain serves to stabilize NOS_{Oxy} and influences
334 redox domain mobility of syNOS in response to Ca^{2+}, akin to the functional role that Ca^{2+}-CAM
335 plays in the regulation of mNOSs. In other systems, Ca^{2+} binding to C2 domains neutralizes
336 acidic regions to allow association with negatively charged phospholipid head-groups (*73*).
337 Although, $syNOS_{C2}$ lacks the typically conserved Asp residues that coordinate Ca^{2+}, isothermal
338 calorimetry (Fig. S17) indicated that the $syNOS_{C2}$ binds Ca^{2+} with a 1.6 μM Kd, which compares
339 to the Ca^{2+} affinity of PLDβ C2 domains (0.8 μM) (*74*).

340 Various stimuli produce surges in cyanobacterial intracellular Ca concentrations from 100-200
341 nm to the μM range (*75*, *76*). In vitro, syNOS activity responds to Ca^{2+} with a K_M of ~ 200 μM
342 (*34*). This larger value may reflect the conformational coupling of the C2 domain movement to
343 Ca^{2+} binding and may be affected by the cellular context. Interestingly, some types of
344 cyanobacteria uptake Ca^{2+} at very high concentrations to mineralize $CaCO_3$ (*77*).

345

346 <u>Ca^{2+} causes a large movement of the C2 domain</u>

347 In the presence of Ca^{2+} and L-arginine, syNOS adopts a more flexible state, wherein most of
348 $syNOS_{Red}$ is undiscerned by cryoEM (NOS-$TO_{L,T}$). In this turnover state, the C2 domain has moved
349 away from the Oxy/FNR interface and now binds at the entrance of the $syNOS_{Glb}$ heme pocket,
350 nearly 85 Å from its original position (Fig. 5A). The new C2 position blocks the $syNOS_{Glb}$ heme-
351 binding center and substantially shifts the αB-D helices and constituent residues that compose
352 the distal heme pocket where NO is oxidized (Fig. 5B). The highly conserved C2 basic patch
353 (Lys35, Lys37 and Arg81) that formally bound $syNOS_{FNR}$ in the locked dimer interacts with the
354 heme-propionic acid groups of $syNOS_{Glb}$ and the 81-89 loop, also conserved among $syNOS_{C2}$
355 domains, reaches over to block the distal heme pocket. Furthermore, the movement of $syNOS_{C2}$
356 displaces the L2 linker, which swivels by ~135° and now directs $syNOS_{Fld}$ toward the backside of
357 the heme pocket on the opposing subunit (Fig. 5C), consistent with the trans ET mechanism
358 characteristic of mNOSs (*58*). As $syNOS_{C2}$ now resides where the electron-donating FNR
359 modules of Hmps interact with their cognate globin domains, we tested whether removal of the
360 C2 domain ($syNOS_{\Delta C2}$) affected $syNOS_{Glb}$ reduction in $syNOS_{FL}$. Surprisingly, we observed little
361 change in $syNOS_{Glb}$ reduction rates in $syNOS_{\Delta C2,}$ nor did Ca^{2+} affect $syNOS_{Glb}$ reduction rates in
362 $syNOS_{FL}$ (Fig. S18).

363

364 <u>$syNOS_{Glb}$ reduction requires an altered configuration of $syNOS_{FNR}$</u>

365 Flavohemoglobins reductively activate dioxygen with an FNR domain in order to oxidize NO to
366 NO_3^-; however, in principle, either $syNOS_{Fld}$ or $syNOS_{FNR}$ could reduce $syNOS_{Glb}$. In the locked

367 state, both the $syNOS_{Fld}$ FMN and the $syNOS_{FNR}$ FAD are too far from the $syNOS_{Glb}$ Fe^{3+} to yield
368 reasonably fast ET rates (27 Å and 31 Å, respectively). When considering that $syNOS_{Glb}$ has a
369 lower potential ($E^{0'}$ = -250 mV) than $syNOS_{Fld}$ (E_m = -170 mV), but not $syNOS_{FNR}$ (E_m = -290 mV),
370 $syNOS_{FNR}$ is likely the better electron donor. However, the relatively low expected driving force
371 for reduction between $syNOS_{FNR}$ and $syNOS_{Glb}$ (Table S5) and a distance of separation of ~31 Å,
372 suggests that $syNOS_{FNR}$ displaces from its position in NOS-Sym to reduce $syNOS_{Glb}$ at the
373 observed rate (Fig. 6; (*78*)). Indeed, the isolated $syNOS_{FNR}$ domain reduces the $syNOS_{Glb}$ domain
374 with saturation behavior (K_m = 11.5 μM) at nearly the same rate (k_{cat} = 0.25 s^{-1}) as $syNOS_{Glb}$ is
375 reduced in full-length Ca^{2+}-free syNOS (k_{obs} = 0.22 s^{-1}, Fig. S18). Furthermore, if $syNOS_{Fld}$ in the
376 locked confirmation can directly reduce $syNOS_{Glb}$, we would expect the conformationally
377 destabilized $syNOS_{\Delta C2}$ to show slower $syNOS_{Glb}$ reduction, but this is not the case (Fig. S16). A
378 modest decrease in syNOS NOD activity with Ca^{2+} suggests an inhibitory effect of $syNOS_{C2}$ (Fig.
379 S18), which would be expected from its relocation to the site where FNR domains typically bind
380 globin domains in Hmps.

381

382 <u>The asymmetric state may act as a conformational intermediate between NOS and NOD</u>
383 <u>activities</u>

384 The mNOS input, intermediate, and output states are not discrete, but sampled within a
385 continuum of motion (*18*, *35*). In the output state, Fld-CAM moves 70 Å to dock onto an
386 opposing NOS_{Oxy} domain at the backside of the heme pocket. Similarly, syNOS-Asym (
387 PDB:9Q0Y,9Q15) represents an intermediate structural state between the locked dimer and the
388 turnover state that is likely in dynamic equilibrium with NOS-Sym and NOS-TO. An Alphafold3
389 prediction of the Oxy dimer unit with one Fld domain places $syNOS_{Fld}$ at the experimentally
390 validated position on $syNOS_{Oxy}$ found by HDX-MS and crosslinking studies of mNOS (*38*). Upon
391 superimposing this prediction onto either NOS-Asym or NOS-Sym, the Fld binding surface on
392 $syNOS_{Oxy}$ is blocked by the $syNOS_{C2}$ (Fig. 5C and S19). Furthermore, compared to Hmp,
393 $syNOS_{FNR}$ would have to rotate 90° and move 28 Å to reduce $syNOS_{Glb}$ (Fig. 6). This configuration
394 is likely accessible in the dynamic asymmetric subunit but would be prevented in $syNOS_{TO}$

395 (PDB:9Q0X) by the rearranged $syNOS_{C2}$. Hence, it is likely that syNOS-Asym is capable of
396 $syNOS_{Glb}$ reduction but not $syNOS_{Oxy}$ reduction.

397 The intermediate conformation of syNOS-Asym (PDB:9Q0Y,9Q15) may be important for the
398 switch between NOS and NOD activities and explain the inhibitory effect of Ca^{2+} on Cc-
399 reduction. In the absence of Ca^{2+}, syNOS-Sym locks down and inhibits NOS activity, but NOS-
400 Asym allows $syNOS_{FNR}$ to reduce $syNOS_{Glb}$, and $syNOS_{Fld}$ to reduce Cc. In syNOS-Asym
401 (PDB:9Q0Y,9Q15), $syNOS_{Fld}$ cannot reduce $syNOS_{Oxy}$ because $syNOS_{C2}$ blocks $syNOS_{Fld}$ from the
402 $syNOS_{Oxy}$ interaction site on the opposing subunit. Ca^{2+} promotes the relocation of the C2
403 domain from $syNOS_{Oxy}$ to $syNOS_{Glb}$; however, some C2 displacement from NOS_{Oxy} may occur in
404 the absence of Ca^{2+} because the C2 domain is not well defined in the more mobile subunit of
405 syNOS-Asym. In addition to preventing $syNOS_{FNR}$ from reducing the $syNOS_{Glb}$, C2 movement
406 disrupts L2, destabilizing the interaction of $syNOS_{Fld}$ with $syNOS_{FNR}$ and favors partitioning of
407 $syNOS_{Fld}$ toward the unblocked $syNOS_{Oxy}$ and away from Cc (Fig. 7).

408 Similar to mNOS, syNOS assumes a continuum of conformations that circumscribe defined
409 enzymatic states. Hence to generate changes in physiologically relevant activities, the relative
410 weighting of states within the conformational ensemble must be regulated and responsive to
411 cellular context. It is striking that the $syNOS_{C2}$ moves between a location that blocks $syNOS_{Oxy}$
412 reduction to one that blocks $syNOS_{Glb}$ reduction, thereby suggesting counter regulation of NO
413 synthesis and NO oxidation. Such a mechanism may allow the enzyme to tune the balance of
414 NO production versus NO detoxification, which would be of benefit for signal transduction,
415 nitrogen metabolism and cellular homeostasis. Overall, these syNOS structural studies
416 demonstrate how a multidomain reductase and its associated regulatory components can
417 undergo large scale rearrangements to modulate reactivity in response to environmental
418 conditions.

419

420 **Methods**

421 **Molecular cloning**

422 The native coding sequence for full-length syNOS (Uniprot ID : B4WU43**)** was PCR-amplified and
423 cloned into a modified pet28-a construct between restriction sites NdeI and XhoI using
424 NEBuilder HiFi DNA Assembly master mix (E2621L). The construct contained sequences for an
425 N-terminal Twin-Strep Tag with a TEV cleavage site. To produce the hptG and gapA construct,
426 htpG and gapA were amplified from K-12 *E. coli* and placed into the MCS-1 and the MCS2 of a
427 tagless pAYC-Duet vector using NEBuilder HiFi DNA Assembly master mix (E2621L). Individual
428 point mutants were constructed using Kinase-Ligase-DpnI (KLD) method using primers in Table
429 S4 (New England Biosciences). All plasmid molecular cloning and plasmid material generation
430 were carried out with NEB® 5-alpha competent *E. coli* (New England Biosciences). Successful
431 transformants were validated through Sanger Sequencing or Nanopore sequencing (Eurofins
432 Genomics).

433 **Protein expression and purification**

434 SyNOS and/or variants were expressed in BL21(DE3) as previously described (*34*) with the
435 modification of co-expression with hptG/gapA, which improved yield and reproducibility. Cell
436 pellets were stored at -80 ^{o}C prior to purification. The pellet was thawed and resuspended in
437 lysis buffer (50 mM HEPES (pH 7.5), 150 mM NaCl, 1 mM TCEP, 10% glycerol and 10 uM BH_4),
438 followed by high-speed centrifugation at 100 000 G and application on Strep-Tactin XT 4-Flow
439 resin (IBA Life Sciences). Elution of the affinity-bound protein fraction was carried out in batch
440 with 50 mM biotin supplemented lysis buffer. Post elution samples were concentrated using
441 Viva-Spin columns (100 kDa cut -off), before application onto 10/300 Superose 6 Increase
442 Column (Cytiva) using Gel Filtration Buffer 1 (GFB1, 25 mM HEPES (pH 7.5), 150 mM NaCl, 1 mM
443 TCEP, 10% glycerol and 10 uM BH_4).

444 **Size exclusion chromotography - Small angle X-ray scattering (SEC-SAXS)**

445 All SEC-SAXS was performed at ID7A1 beamline at Cornell High Energy Synchrotron Source
446 (CHESS). Photon flux was 2.3 x 10^{12} ph/s and scattering data was collected 0.005 $Å^{-1} \leq q \leq 0.7$ $Å^{-1}$
447 on an EIGER 4M detector (Dectris). Samples were injected into an inline 3.2/150 Superdex 200
448 column in gel filtration buffer. The entire SEC-SAXS trace was captured using a 2s per exposure
449 throughout the elution. The flow-cell format of the experiment should limit x-ray

450 photoreduction of the sample, but it is possible that the NOS cofactors undergo some
451 photoreduction during the experiment (*79*). All SEC-SAXS data processing was performed
452 through RAW (*80*).

453 **Single turnover anaerobic globin reduction**

454 Anerobic $syNOS_{Glb}$ heme reduction assays were carried out using an Agilent 8453 UV-Vis
455 spectrometer with an attached Hewlett Packard 89090A Peltier temperature controller for
456 maintaining constant temperature at 20 ^{o}C and constant stirring at 400 rpm (Agilent & Hewlett
457 Packard). Prior to reaction initiation with 1 mM NADPH, syNOS or variants (1 µM) were
458 incubated anaerobically in the presence of the Glucose Oxidase/Catalase (GOD/CAT) oxygen
459 scavenging system, as previously described (*81*). Samples were run in either in the presence of 1
460 mM Ca^{2+} or 1 mM EGTA, as noted. In the case of $syNOS_{FNR}$ (1027-1468)/$syNOS_{Glb}$ (337-469)
461 reduction trials, $syNOS_{Glb}$ was fixed at 2.2 µM and $syNOS_{FNR}$ was varied between 1 µM to 21 µM
462 with no EGTA/Ca^{2+} present. All data was processed using home-made scripts in R Studio (Posit
463 PBC) with rates of $syNOS_{Glb}$ reduction with to a single exponential to determine k_{obs}. For the
464 truncated domains k_{cat} and K_m were calculated by plotting k_{obs} for each $syNOS_{FNR}$/$syNOS_{Glb}$ pair
465 against $syNOS_{FNR}$ concentration using Prisim (GraphPad).

466 **Stopped-flow pre-steady state flavin reduction kinetics**

467 Anerobic stopped-flow mixing of NADPH with $syNOS_{Red}$ or $syNOS_{Fl}$ in the absence of Ca^{2+} was
468 used to characterize flavin reduction rates. After purification, $syNOS_{Red}$ contains oxidized FAD
469 and FMN. Attempts to pre-reduce the enzyme to FMNH• with sodium dithionate, DTT and
470 ascorbate caused precipitation without an observable spectral shift to FMNH•. Thus, flavin
471 reduction rates reflect conversion from fully oxidized $syNOS_{Red}$. All stopped flow experiments
472 were carried out anaerobically using a Stopped Flow SX20 instrument (Applied Photophysics).
473 Samples were pre-incubated anaerobically in the presence of the GOD/CAT oxygen scavenging
474 system (see above). Changes in absorbance were detected using a single wavelength
475 Photomultiplier Tube detector. $syNOS_{FL}$ (10 µM) / $syNOS_{Red}$ (40 µM) were mixed with 4x excess
476 NADPH. All data was processed using home-made scripts in R Studio (Posit PBC).

477 **CryoEM grid preparation and data collection - syNOS ligand free (Dataset 1 and 2)**

478 A 4 µl volume of 1.0 mg ml^{-1} syNOS solution, in GFB1, was applied to glow-discharged grids (200
479 mesh Quantifoil Cu, R1.2/1.3; Electron Microscopy Sciences). After 10 s of incubation, the
480 excess solution was blotted for 3.5 s with filter paper by a Vitrobot Mark IV and plunged into
481 liquid ethane, for vitrification (ThermoFisher). CryoEM images of syNOS were collected on a
482 Talos Arctica (ThermoFisher) operated at 200 keV at a nominal magnification of 63,000× with a
483 Gatan GIF Quantum LS Imaging energy filter, using a Gatan K3 direct electron camera in super-
484 resolution counting mode, corresponding to a pixel size of 1.31 Å. A total of 1214 images stacks
485 were obtained with a defocus range of −0.8 to −2.0 µm by Serial EM (University of Colorado-
486 Boulder). Each stack video was recorded for a total dose of 50 electrons per Å^2.

487 **CryoEM grid preparation and data collection - Ca^{2+} and L-arginine conditions (Dataset 3)**

488 A 4 µl volume of 1.0 mg ml^{-1} syNOS in the presence of 1 mM Ca^{2+} and 1 mM L-arg solution was
489 applied to glow-discharged grids (300 mesh Quantifoil Au, R1.2/1.3). After 10s of incubation, the
490 excess solution was blotted for 2.5 s with filter paper by a Vitrobot Mark IV and plunged into
491 liquid ethane for vitrification (ThermoFisher). CryoEM images of syNOS were collected on a
492 Talos Krios (ThermoFisher) operated at 300 keV at a nominal magnification of 165,000× with a
493 Gatan GIF Quantum LS Imaging energy filter, using a Gatan K3 direct electron camera in super-
494 resolution counting mode, corresponding to a pixel size of 0.422 Å. A total of 5019 images stacks
495 were obtained with a defocus range of −0.6 to −2.0 µm by Leginon (*82*). Each stack video was
496 recorded for a total dose of 50.5 electrons per Å^2.

497 **CryoEM grid preparation and data collection - turnover conditions (Dataset 5)**

498 A 4 µl volume of 1.0 mg ml^{-1} syNOS-ligand free solution in GFB1 was applied to glow-discharged
499 grids (200 mesh Quantifoil Cu, R1.2/1.3). After 10s of incubation, the excess solution was
500 blotted for 3.5 s with filter paper by a Vitrobot Mark IV and plunged into liquid ethane for
501 vitrification (ThermoFisher). CryoEM images of syNOS were collected on a Talos Krios
502 (ThermoFisher) operated at 300 keV at a nominal magnification of × 165,000 with a Gatan GIF
503 Quantum LS Imaging energy filter, using a Gatan K3 direct electron camera in super-resolution
504 counting mode, corresponding to a pixel size of 0.730 Å. A total of 5001 images stacks were

505 obtained with a defocus rage of −0.6 to −2.0 µm by Leginon (*82*). Each stack video was recorded
506 for a total dose of 44.9 electrons per $Å^2$.

507 **CryoEM Image processing and structural reconstruction**

508 All cryoEM density refinement was performed using CryoSPARC (*50*). In brief, micrograpghs
509 were motion corrected using patch motion followed by CTF estimation using patch CTF. Particles
510 were picked using CRYOLO and run through 2D classification and initial density reconstructions.
511 Candidate densities were then selected for further refinement, including junk classes to
512 eliminate contaminating/damaged particles. For dataset dependant details please refer to Figs
513 .S2-S6. as illustrated by the procedures illustrated in Figs. S2-S6.

514 For syNOS-Asym (DS4, EMD-72110), non-uniform refinement obscured the smaller subunit. To
515 improve the density quality we locally refined each subunit. ChimeraX was used to create the
516 two masks, centered at each subunit, for the local refinement(Fig. S5). Gaussian noise with a
517 standard deviation of 3 was applied to EMD 72110, producing a new density that obscured
518 secondary structure features. The Segger tool (*83*) was used to segment the map into each
519 subunit. composite map (EMD-72116) produced from DS4, The electron density was resampled
520 into the appropriate box size and imported into CryoSPARC where masks were created using the
521 3D Volume tool and subsequently used for local refinement. The refined maps were aligned and
522 merged using the vop maximum command in ChimeraX to produce the composite map.

523 An Alphafold3 prediction of a syNOS homodimer (residues 1-1468), was used as the input
524 model and docked into the appropriate electron density using ChimeraX (*50*, *84*, *85*). Ligand and
525 poor fitting regions were built and real-space refined using with Coot (*85*). The resulting models
526 were passed through ISOLDE (*86*) to approach thermodynamically rational
527 rotamers/conformations. The outputs from these initial models were subjected to a series of
528 real-space refinement with PHENIX (*87*) and conformational outlier residues were then adjusted
529 manually using Coot (*85*).

530 **Cytochrome c reduction assay**

531 Cytochrome c (Cc) was used as an electron acceptor to measure the efficiency of electron flow
532 from NOS_{Red}. Cc accepts an electron from the fully reduced $FMNH_2$ and not from $FADH_2$/$FADH^{-\bullet}$/$FAD^{\bullet}$/ $FMNH^{\bullet}$. Cc reduction assays were carried out as previously described (*88*) using an
534 Agilent 8453 UV-Vis Spectrometer with an attached Hewlett Packard 89090A Peltier
535 Temperature Controller for constant temperature at 20 ^{o}C and constant stirring at 400 rpm
536 (Agilent & Hewlett Packard). All reported reactions were carried out in CC buffer (100 mM Tris
537 (pH 7.5) and 200 mM NaCl). Cc was pre-oxidized with 1 mM potassium ferrocyanide and then
538 buffer exchanged into CC buffer. Reactions were conducted with 10 uM Cc and 3 nM of the
539 sample of interest. Reactions were initiated with 1 mM NADPH and were run either in the
540 presence of 1 mM Ca^{2+} or 1 mM EGTA as noted. All data was processed using home-made
541 scripts in R Studio (Posit PBC).

542 **Nitric oxide synthase activity assay**

543 All activity assays were carried out for 30 minutes in 100 mM Tris, (pH 7.5) 200 mM NaCl, 1 mM
544 DTT and 1 mM L-arginine and initiated with 1 mM NADPH (25 °C). Each sample was evaluated in
545 the presence of 1 mM Ca^{2+} or 1 mM EGTA. Post reaction, samples were boiled at 70 ^{o}C to halt
546 NOS activity. NADPH was then precipitated using the $ZnCl_2$/$NaCO_3$ method and subsequently
547 centrifuged at 15000 G at room temperature. The supernatant was then quantified for total
548 NO_2^- and NO_3^- content through the Griess assay as implemented in the Nitrate/Nitrite
549 Colorimetric Assay Kit (Cayman Chemicals).

550 **Oxygen consumption assay to probe Nitric Oxide Dioxygenase activity**

551 The Oxygraph+ system (Hansatech Instruments) was used to measure oxygen consumption of
552 syNOS in the presence of the NO donor, 3-(2-Hydroxy-1-methyl-2-nitrosohydrazino)-N-methyl-1-
553 propanamine (NOC-7). 1 µM of enzyme ($syNOS_{Fl}$ or $syNOS_{\Delta C2}$) was incubated in buffer
554 containing 50 mM Tris and 150 mM NaCl at pH 7.5, with 10 µM NOC-7 for 5 minutes. The
555 reaction was initiated with 1 mM NADPH. Each sample was evaluated in the presence of 1 mM
556 Ca^{2+} or 1 mM EGTA . Three separate controls were performed to rule out superoxide or non-
557 enzymatic NO oxidation: NOC-7 + NADPH, NOC-7 + $syNOS_{FL}$ and syNOS + NADPH.

558 **Isothermal calorimetry**

559 Thermodynamic binding properties between Ca^{2+} and $syNOS_{C2}$ (1-138) were measured on a
560 Nano ITC Low Volume isothermal titration calorimeter (TA instruments). $SyNOS_{C2}$ was prepared
561 in a 50 mM CHES and 150 mM NaCl buffer at pH 9.0 at 0.072 mM with 200 µL in the sample cell.
562 Lower pHs also gave indication of Ca^{2+} binding, but led to aggregation of the C2 domain that
563 prevented quantitative assessment. $CaCl_2$ was prepared in the same buffer at a concentration of
564 0.250 mM; 2.5uL was titrated every 250 s for a total of 30 injections. Thermal data were
565 analyzed using an independent binding model with the NanoAnalyze software.

566 **Reduction potential determination**

567 Measurements were performed using the isolated domains $syNOS_{Glb}$ (337-469), $syNOS_{FMN}$ (856-
568 1027) and $syNOS_{FNR}$ (1027-1468), which were expressed and purified separately. Reduction
569 potential measurements were performed using a dye calibration method (*89*, *90*), wherein
570 reduction was driven by a deazaflavin/EDTA photochemical system in a 50 mM $NaPO_3$, 10%
571 Glycerol at pH 7.0, with the following modifications: i) 9 µm 5-deazariobflavin and 5 mM EDTA
572 was used as the chemical reductant ii) reactions were equilibrated anaerobically in a coy
573 chamber while supplemented with GOD/CAT oxygen scavenging system. All measurements
574 were carried out using an Agilent 8453 UV-Vis spectrometer with an attached Hewlett Packard
575 89090A Peltier Temperature Controller for maintaining constant temperature at 20 ^{o}C and
576 constant stirring at 400 rpm (Agilent & Hewlett Packard), with the reaction being photoinitiated
577 with a 15 mW 300 nm laser (ThorLabs) placed above the clear septum capping the cuvette.
578 Calibrating dyes per domain were selected based on literature values of the published redox
579 potentials (Table S5). Note that the quoted reduction potentials for $syNOS_{Fld}$ and $syNOS_{FNR}$ will
580 be the average of the single electron couples between semiquinone and oxidized, and
581 hydroquinone and semiquinone.

582 **DSBU crosslinking, in-gel protein digestion and extraction**

583 Purified syNOS that correspond to the dimer fraction from SEC was split into two conditions: 1)
584 inactive - GFB1, 2) turnover - GFB1 + 1mM Ca^{2+} + 1 mM NADPH + 100 µM BH_4. Both conditions
585 were then incubated with 1mM (100 molar excess) disuccinimidyl dibutyric urea (DSBU,

586 ThermoFisher) for 30 minutes at room temperature prior to quenching with 20 mM Tris pH 8.0.
587 Samples were then centrifuged and run on an SDS-PAGE gel using lameli sample buffer.

588 Bands corresponding to dimers were excised, digested and extracted as previously described
589 (*91*), apart from the proteases of choice being Lys-C/Trypsin, prior to LC- MS/MS analysis.

590 **Crosslinks identification by nanoLC-MS/MS**

591 The digested product was characterized by NanoLC-MS/MS analysis at the Cornell
592 Biotechnology Resource Center. The analysis was carried out using an Orbitrap FusionTM
593 TribridTM (Thermo-Fisher Scientific, San Jose, CA) mass spectrometer equipped with a
594 nanospray Flex Ion Source, and coupled with a Dionex UltiMate 3000 RSLCnano system
595 (Thermo, Sunnyvale, CA). Each sample was loaded onto a nano Viper PepMap C18 trapping
596 column (5 µm, 100 µm ´ 20 mm, 100 Å, Thermo Fisher Scientific) at 20 L/min flow rate for rapid
597 sample loading. After 3 minutes, the valve switched to allow peptides to be separated on an
598 Acclaim PepMap C18 nano column (2 µm, 75 µm x 25 cm, Thermo Fisher Scientific) at 35 °C in a
599 93 min gradient of 5% to 40% then 93-98 min of 40%-60% buffer B (95% ACN with 0.1% formic
600 acid) at 300 nL/min. The Orbitrap Fusion was operated in positive ion mode with nano spray
601 voltage set at 1.5 kV and source temperature at 275 °C. External calibrations for Fourier
602 transform, ion-trap and quadrupole mass analyzers were performed prior to the analysis.
603 Samples were analyzed using the HCD-MS2 workflow, in which MS scan range was set to 300-
604 1800 m/z and the resolution was set to 60,000. Precursor ions with charge states 2-8 were
605 selected for HCD MS2 acquisitions in Orbitrap analyzer with a resolution of 30,000 with collision
606 energy of 25% and 30%, normalized AGC of 200%. The precursor isolation width was 1.6 m/z
607 and the maximum injection time was 70 ms. All data were acquired under Xcalibur 4.4
608 operation software (Thermo-Fisher Scientific).

609 **Crosslink identification and visualization**

610 Raw spectra were searched using Proteome Discoverer 2.4 (Thermo-Fisher Scientific, San Jose,
611 CA) with XlinkX v2.0 algorithm for identification of crosslinked peptides. The search parameters
612 were as follow: four missed cleavages for either double digestion or triple digestion with fixed
613 carbamidomethyl modification of cysteine, variable modifications of methionine oxidation,

614 asparagine/glutamine deamidation, protein N-terminal acetylation, serine/threonine/tyrosine
615 phosphorylation and lysine di-glycine tag . Only lysine-to-lysine crosslinks were considered. The
616 peptide mass tolerance was 10 ppm, and MS2 fragment mass tolerance was 0.6 Da. A custom
617 database (246 sequences) containing syNOS, common *E.coli* chaperones and common
618 contaminates was used for the search, with > 1% FDR for report of crosslink results. Identified
619 crosslinked peptides were filtered for Max. XlinkX Score > 40, a confidence score that reflects
620 how well peptide spectrum matching, peptide fragmentation and crosslink doublet
621 identification. Spectra were manually analyzed to validate potential crosslinks. The crosslinked
622 peptides were analyzed using XMAS (*93*).
623

624 **References**

625 1. R. M. Palmer, S. Moncada, A novel citrulline-forming enzyme implicated in the formation of
626 nitric oxide by vascular endothelial cells. *Biochem Biophys Res Commun* **158**, 348–352
627 (1989).

628 2. B. R. Crane, Bacterial Nitric Oxide Synthases. *Annual Review Of Biochemistry* **79** (2010).

629 3. J. A. McCleverty, Chemistry of Nitric Oxide Relevant to Biology. *Chem. Rev.* **104**, 403–418
630 (2004).

631 4. M. Cossenza, R. Socodato, C. C. Portugal, I. C. L. Domith, L. F. H. Gladulich, T. G. Encarnaçao,
632 K. C. Calaza, H. R. Mendonça, P. Campello-Costa, R. Paes-de-Carvalho, "Nitric Oxide in the
633 Nervous System: Biochemical, Developmental, and Neurobiological Aspects" in *Nitric*
634 *Oxide*, G. Litwack, Ed. (2014)vol. 96 of *Vitamins and Hormones*, pp. 79–125.

635 5. C. Farah, L. Y. M. Michel, J. L. Balligand, Nitric oxide signalling in cardiovascular health and
636 disease. *Nature Reviews Cardiology* **15**, 292–316 (2018).

637 6. J. O. Lundberg, E. Weitzberg, Nitric oxide signaling in health and disease. *Cell* **185**, 2853–
638 2878 (2022).

639 7. M. A. Marletta, Revisiting Nitric Oxide Signaling: Where Was It, and Where Is It Going?
640 *Biochemistry* **60**, 3491–3496 (2021).

641 8. M. Shepherd, D. Giordano, C. Verde, R. K. Poole, The Evolution of Nitric Oxide Function:
642 From Reactivity in the Prebiotic Earth to Examples of Biological Roles and Therapeutic
643 Applications. *Antioxidants* **11** (2022).

644 9. K. A. White, M. A. Marletta, Nitric oxide synthase is a cytochrome P-450 type hemoprotein,
645 *ACS Publications* (2002). https://doi.org/10.1021/bi00144a001.

646 10. U. Förstermann, W. C. Sessa, Nitric oxide synthases: regulation and function. *Eur Heart J*
647 **33**, 829–837, 837a–837d (2012).

648 11. M. A. Cinelli, H. T. Do, G. P. Miley, R. B. Silverman, Inducible nitric oxide synthase:
649 Regulation, structure, and inhibition. *Med Res Rev* **40**, 158–189 (2020).

650 12. D. J. Stuehr, M. M. Haque, Nitric oxide synthase enzymology in the 20 years after the Nobel
651 Prize. *British Journal of Pharmacology* **176**, 177–188 (2019).

652 13. J. Reyes-Rivera, Y. Wu, B. G. H. Guthrie, M. A. Marletta, N. King, T. Brunet, Nitric oxide
653 signaling controls collective contractions in a colonial choanoflagellate. *Curr Biol* **32**, 2539-
654 2547.e5 (2022).

655 14. J. Tejero, D. Stuehr, Tetrahydrobiopterin in nitric oxide synthase. *IUBMB Life* **65**, 358–365
656 (2013).

657 15. D. J. Stuehr, J. Santolini, Z.-Q. Wang, C.-C. Wei, S. Adak, Update on mechanism and catalytic
658 regulation in the NO synthases. *J Biol Chem* **279**, 36167–36170 (2004).

659 16. H. M. Abu-Soud, D. J. Stuehr, Nitric oxide synthases reveal a role for calmodulin in
660 controlling electron transfer. *Proc Natl Acad Sci U S A* **90**, 10769–10772 (1993).

661 17. D. H. Craig, S. K. Chapman, S. Daff, Calmodulin Activates Electron Transfer through
662 Neuronal Nitric-oxide Synthase Reductase Domain by Releasing an NADPH-dependent
663 Conformational Lock *. *Journal of Biological Chemistry* **277**, 33987–33994 (2002).

664 18. N. G. H. Leferink, S. Hay, S. E. J. Rigby, N. S. Scrutton, Towards the free energy landscape for
665 catalysis in mammalian nitric oxide synthases. *The FEBS Journal* **282**, 3016–3029 (2015).

666 19. T. L. Poulos, H. Li, Nitric Oxide Synthase and Structure-Based Inhibitor Design. *Nitric Oxide*
667 **63**, 68–77 (2017).

668 20. L. Zhou, D.-Y. Zhu, Neuronal nitric oxide synthase: Structure, subcellular localization,
669 regulation, and clinical implications. *Nitric Oxide* **20**, 223–230 (2009).

670 21. V. Garcia, W. C. Sessa, Endothelial NOS: perspective and recent developments. *Br J*
671 *Pharmacol* **176**, 189–196 (2019).

672 22. N. A. Popova, S. K. Soodaeva, I. A. Klimanov, V. M. Misharin, A. A. Temnov, Autoregulation
673 and Autoinhibition of the Main NO Synthase Isoforms (Brief Review). *Sovremennye*
674 *Tehnologii V Medicine* **15**, 53–59 (2023).

675 23. M. C. Surdel, B. F. Dutter, G. A. Sulikowski, E. P. Skaar, Bacterial Nitric Oxide Synthase Is
676 Required for the Staphylococcus aureus Response to Heme Stress. *ACS Infect. Dis.* **2**, 572–
677 578 (2016).

678 24. I. Gusarov, K. Shatalin, M. Starodubtseva, E. Nudler, Endogenous Nitric Oxide Protects
679 Bacteria Against a Wide Spectrum of Antibiotics. *Science* **325**, 1380–1384 (2009).

680 25. B. A. Patel, M. Moreau, J. Widom, H. Chen, L. Yin, Y. Hua, B. R. Crane, Endogenous nitric
681 oxide regulates the recovery of the radiation-resistant bacterium Deinococcus radiodurans
682 from exposure to UV light. *Proc Natl Acad Sci U S A* **106**, 18183–18188 (2009).

683 26. N. Gupta, A. Srivastava, A. K. Mishra, Nitric Oxide Synthases in Cyanobacteria: Diversity,
684 Cellular Implications and Ecological Pertinence. *J Plant Growth Regul* **44**, 508–528 (2025).

685 27. T. G. Popova, A. Teunis, H. Vaseghi, W. Zhou, V. Espina, L. A. Liotta, S. G. Popov, Nitric oxide
686 as a regulator of *B-anthracis* pathogenicity. *Frontiers in Microbiology* **6** (2015).

687 28. P. R. Gardner, Nitric oxide dioxygenase function and mechanism of flavohemoglobin,
688 hemoglobin, myoglobin and their associated reductases. *J Inorg Biochem* **99**, 247–266
689 (2005).

690 29. P. R. Gardner, A. M. Gardner, L. A. Martin, A. L. Salzman, Nitric oxide dioxygenase: An
691 enzymic function for flavohemoglobin. *Proceedings of the National Academy of Sciences*
692 **95**, 10378–10383 (1998).

693 30. M. E. S. Lewis, H. A. Corker, B. Gollan, R. K. Poole, "A survey of methods for the purification
694 of microbial flavohemoglobins" in *Globins and Other Nitric Oxide-Reactive Proteins, Pt A*, R.
695 K. Poole, Ed. (2008)vol. 436 of *Methods in Enzymology*, pp. 169–186.

696 31. F. Del Castello, N. Foresi, A. Nejamkin, C. Lindermayr, F. Buegger, L. Lamattina, N. Correa-
697 Aragunde, Cyanobacterial NOS expression improves nitrogen use efficiency, nitrogen-
698 deficiency tolerance and yield in Arabidopsis. *Plant Science* **307** (2021).

699 32. N. Correa-Aragunde, N. Foresi, F. Del Castello, L. Lamattina, A singular nitric oxide synthase
700 with a globin domain found in Synechococcus PCC 7335 mobilizes N from arginine to
701 nitrate. *Sci Rep* **8**, 12505 (2018).

702 33. M. M. Labarthe, G. A. Maroniche, L. Lamattina, C. M. Creus, Nitric oxide synthase
703 expression in Pseudomonas koreensis MME3 improves plant growth promotion traits.
704 *Appl. Microbiol. Biotechnol.* **108** (2024).

705 34. A. L. Picciano, B. R. Crane, A nitric oxide synthase-like protein from Synechococcus
706 produces NO/NO3- from l-arginine and NADPH in a tetrahydrobiopterin- and Ca2+-
707 dependent manner. *J Biol Chem* **294**, 10708–10719 (`).

35. M. G. Campbell, B. C. Smith, C. S. Potter, B. Carragher, M. A. Marletta, Molecular architecture of mammalian nitric oxide synthases. *Proc Natl Acad Sci U S A* **111**, E3614-3623 (2014).

36. D. Felker, K. Lee, T. H. Pospiech, Y. Morishima, H. Zhang, M. Lau, D. R. Southworth, Y. Osawa, Mapping interactions of calmodulin and neuronal NO synthase by crosslinking and mass spectrometry. *Journal of Biological Chemistry* **300** (2024).

37. A. L. Yokom, Y. Morishima, M. Lau, M. Su, A. Glukhova, Y. Osawa, D. R. Southworth, Architecture of the nitric-oxide synthase holoenzyme reveals large conformational changes and a calmodulin-driven release of the FMN domain. *J Biol Chem* **289**, 16855–16865 (2014).

38. B. C. Smith, E. S. Underbakke, D. W. Kulp, W. R. Schief, M. A. Marletta, Nitric oxide synthase domain interfaces regulate electron transfer and calmodulin activation. *Proc Natl Acad Sci U S A* **110**, E3577-3586 (2013).

39. T. Jiang, M. C. Thielges, C. J. Feng, Emerging approaches to investigating functional protein dynamics in modular redox enzymes: Nitric oxide synthase as a model system. *J. Biol. Chem.* **301** (2025).

40. C. R. Pudney, D. J. Heyes, B. Khara, S. Hay, S. E. J. Rigby, N. S. Scrutton, Kinetic and spectroscopic probes of motions and catalysis in the cytochrome P450 reductase family of enzymes. *Febs Journal* **279**, 1534–1544 (2012).

41. T. M. Hedison, N. G. H. Leferink, S. Hay, N. S. Scrutton, Correlating Calmodulin Landscapes with Chemical Catalysis in Neuronal Nitric Oxide Synthase using Time-Resolved FRET and a 5-Deazaflavin Thermodynamic Trap. *Acs Catalysis* **6**, 5170–5180 (2016).

42. T. M. Hedison, S. Hay, N. S. Scrutton, Trapping methods for probing functional intermediates in nitric oxide synthases and related enzymes. *Frontiers in Bioscience-Landmark* **23**, 1874–1888 (2018).

43. Y. He, M. M. Haque, D. J. Stuehr, H. P. Lu, Conformational states and fluctuations in endothelial nitric oxide synthase under calmodulin regulation. *Biophysical Journal* **120**, 5196–5206 (2021).

44. J. Li, H. Zheng, C. Feng, Deciphering mechanism of conformationally controlled electron transfer in nitric oxide synthases. *Frontiers in Bioscience-Landmark* **23**, 1803–1821 (2018).

45. C. J. Feng, Mechanism of nitric oxide synthase regulation: Electron transfer and interdomain interactions. *Coordination Chemistry Reviews* **256**, 393–411 (2012).

46. D. J. Stuehr, J. Tejero, M. M. Haque, Structural and mechanistic aspects of flavoproteins: electron transfer through the nitric oxide synthase flavoprotein domain. *The FEBS Journal* **276**, 3959–3974 (2009).

743 47. M. M. Haque, C. Kenney, J. Tejero, D. J. Stuehr, A kinetic model linking protein
744 conformational motions, interflavin electron transfer and electron flux through a dual-
745 flavin enzyme-simulating the reductase activity of the endothelial and neuronal nitric oxide
746 synthase flavoprotein domains. *FEBS J* **278**, 4055–69 (Nov).

747 48. R. Chakravarti, K. S. Aulak, P. L. Fox, D. J. Stuehr, GAPDH regulates cellular heme insertion
748 into inducible nitric oxide synthase. *Proceedings of the National Academy of Sciences* **107**,
749 18004–18009 (2010).

750 49. Y. Morishima, M. Lau, W. B. Pratt, Y. Osawa, Dynamic cycling with a unique Hsp90/Hsp70-
751 dependent chaperone machinery and GAPDH is needed for heme insertion and activation
752 of neuronal NO synthase. *J Biol Chem* **299**, 102856 (2023).

753 50. A. Punjani, J. L. Rubinstein, D. J. Fleet, M. A. Brubaker, cryoSPARC: algorithms for rapid
754 unsupervised cryo-EM structure determination. *Nat Methods* **14**, 290–296 (2017).

755 51. T. Wagner, F. Merino, M. Stabrin, T. Moriya, C. Antoni, A. Apelbaum, P. Hagel, O. Sitsel, T.
756 Raisch, D. Prumbaum, D. Quentin, D. Roderer, S. Tacke, B. Siebolds, E. Schubert, T. R.
757 Shaikh, P. Lill, C. Gatsogiannis, S. Raunser, SPHIRE-crYOLO is a fast and accurate fully
758 automated particle picker for cryo-EM. *Commun Biol* **2**, 218 (2019).

759 52. H. Shi, C. Wu, X. Zhang, Addressing compressive deformation of proteins embedded in
760 crystalline ice. *Structure* **31**, 213-220.e3 (2023).

761 53. B. R. Crane, The enzymology of nitric oxide in bacterial pathogenesis and resistance.
762 *Biochemical Society Transactions* **36**, 1149–1154 (2008).

763 54. K. Pant, A. M. Bilwes, S. Adak, D. J. Stuehr, B. R. Crane, Structure of a nitric oxide synthase
764 heme protein from Bacillus subtilis. *Biochemistry* **41**, 11071–9 (2002).

765 55. B. R. Crane, A. S. Arvai, D. K. Ghosh, C. Wu, E. D. Getzoff, D. J. Stuehr, J. A. Tainer, Structure
766 of nitric oxide synthase oxygenase dimer with pterin and substrate. *Science* **279**, 2121–6
767 (1998).

768 56. S. Corbalan-Garcia, J. C. Gómez-Fernández, Signaling through C2 domains: More than one
769 lipid target. *Biochimica et Biophysica Acta (BBA) - Biomembranes* **1838**, 1536–1547 (2014).

770 57. T. A. Leonard, "C2 Domain Proteins" in *Encyclopedia of Metalloproteins*, R. H. Kretsinger, V.
771 N. Uversky, E. A. Permyakov, Eds. (Springer, New York, NY, 2013;
772 https://doi.org/10.1007/978-1-4614-1533-6_39), pp. 309–318.

773 58. U. Siddhanta, A. Presta, B. Fan, D. Wolan, D. L. Rousseau, D. J. Stuehr, Domain Swapping in
774 Inducible Nitric-oxide Synthase: ELECTRON TRANSFER OCCURS BETWEEN FLAVIN AND
775 HEME GROUPS LOCATED ON ADJACENT SUBUNITS IN THE DIMER*. *Journal of Biological*
776 *Chemistry* **273**, 18950–18958 (1998).

777 59. J. Tejero, M. M. Haque, D. Durra, D. J. Stuehr, A Bridging Interaction Allows Calmodulin to
778 Activate NO Synthase through a Bi-modal Mechanism. *J Biol Chem* **285**, 25941–25949
779 (2010).

780 60. P.-F. Chen, K. K. Wu, Structural elements contribute to the calcium/calmodulin dependence
781 on enzyme activation in human endothelial nitric-oxide synthase. *J Biol Chem* **278**, 52392–
782 52400 (2003).

783 61. E. D. Garcin, C. M. Bruns, S. J. Lloyd, D. J. Hosfield, M. Tiso, R. Gachhui, D. J. Stuehr, J. A.
784 Tainer, E. D. Getzoff, Structural Basis for Isozyme-specific Regulation of Electron Transfer in
785 Nitric-oxide Synthase * [boxs]. *Journal of Biological Chemistry* **279**, 37918–37927 (2004).

786 62. B. Ghazi Esfahani, N. Walia, K. Neselu, Y. Garg, M. Aragon, I. Askenasy, H. A. Wei, J. H.
787 Mendez, M. E. Stroupe, Structure of dimerized assimilatory NADPH-dependent sulfite
788 reductase reveals the minimal interface for diflavin reductase binding. *Nat Commun* **16**,
789 2955 (2025).

790 63. H. Olteanu, R. Banerjee, Human Methionine Synthase Reductase, a Soluble P-450
791 Reductase-like Dual Flavoprotein, Is Sufficient for NADPH-dependent Methionine Synthase
792 Activation *. *Journal of Biological Chemistry* **276**, 35558–35563 (2001).

793 64. Z.-Q. Wang, R. J. Lawson, M. R. Buddha, C.-C. Wei, B. R. Crane, A. W. Munro, D. J. Stuehr,
794 Bacterial flavodoxins support nitric oxide production by Bacillus subtilis nitric-oxide
795 synthase. *J Biol Chem* **282**, 2196–2202 (2007).

796 65. S. Daff, I. Sagami, T. Shimizu, The 42-amino acid insert in the FMN domain of neuronal
797 nitric-oxide synthase exerts control over Ca(2+)/calmodulin-dependent electron transfer. *J*
798 *Biol Chem* **274**, 30589–30595 (1999).

799 66. M. Tiso, J. Tejero, K. Panda, K. S. Aulak, D. J. Stuehr, Versatile regulation of neuronal nitric
800 oxide synthase by specific regions of its C-terminal tail. *Biochemistry* **46**, 14418–28 (2007).

801 67. L. J. Roman, R. T. Miller, M. A. de La Garza, J. J. Kim, B. S. Siler Masters, The C terminus of
802 mouse macrophage inducible nitric-oxide synthase attenuates electron flow through the
803 flavin domain. *J Biol Chem* **275**, 21914–21919 (2000).

804 68. L. J. Roman, P. Martásek, R. T. Miller, D. E. Harris, M. A. de La Garza, T. M. Shea, J. J. Kim, B.
805 S. Masters, The C termini of constitutive nitric-oxide synthases control electron flow
806 through the flavin and heme domains and affect modulation by calmodulin. *J Biol Chem*
807 **275**, 29225–29232 (2000).

808 69. D. Hamdane, C. Xia, S.-C. Im, H. Zhang, J.-J. P. Kim, L. Waskell, Structure and Function of an
809 NADPH-Cytochrome P450 Oxidoreductase in an Open Conformation Capable of Reducing
810 Cytochrome P450*. *Journal of Biological Chemistry* **284**, 11374–11384 (2009).

70. M. Tiso, D. W. Konas, K. Panda, E. D. Garcin, M. Sharma, E. D. Getzoff, D. J. Stuehr, C-terminal Tail Residue Arg1400 Enables NADPH to Regulate Electron Transfer in Neuronal Nitric-oxide Synthase *. *Journal of Biological Chemistry* **280**, 39208–39219 (2005).

71. S. Adak, M. Sharma, A. L. Meade, D. J. Stuehr, A conserved flavin-shielding residue regulates NO synthase electron transfer and nicotinamide coenzyme specificity. *Proceedings of the National Academy of Sciences* **99**, 13516–13521 (2002).

72. E. A. Nalefski, J. J. Falke, The C2 domain calcium-binding motif: structural and functional diversity. *Protein Sci* **5**, 2375–2390 (1996).

73. N. Verdaguer, S. Corbalan-Garcia, W. F. Ochoa, I. Fita, J. C. Gómez-Fernández, Ca2+ bridges the C2 membrane-binding domain of protein kinase Cα directly to phosphatidylserine. *The EMBO Journal* **18**, 6329–6338 (1999).

74. L. Zheng, R. Krishnamoorthi, M. Zolkiewski, X. Wang, Distinct Ca2+ Binding Properties of Novel C2 Domains of Plant Phospholipase Dα and β *. *Journal of Biological Chemistry* **275**, 19700–19706 (2000).

75. M. González-Pleiter, M. Tamayo-Belda, G. Pulido-Reyes, G. Amariei, F. Leganés, R. Rosal, F. Fernández-Piñas, Secondary nanoplastics released from a biodegradable microplastic severely impact freshwater environments. *Environ. Sci.: Nano* **6**, 1382–1392 (2019).

76. I. Torrecilla, F. Leganés, I. Bonilla, F. Fernández-Piñas, Light-to-dark transitions trigger a transient increase in intracellular Ca2+ modulated by the redox state of the photosynthetic electron transport chain in the cyanobacterium Anabaena sp. PCC7120. *Plant, Cell & Environment* **27**, 810–819 (2004).

77. A. De Wever, K. Benzerara, M. Coutaud, G. Caumes, M. Poinsot, F. Skouri-Panet, T. Laurent, E. Duprat, M. Gugger, Evidence of high Ca uptake by cyanobacteria forming intracellular CaCO3 and impact on their growth. *Geobiology* **17**, 676–690 (2019).

78. C. C. Moser, J. M. Keske, K. Warncke, R. S. Farid, P. L. Dutton, Nature of biological electron transfer. *Nature* **355**, 796–802 (1992).

79. W.-C. Huang, J. Ellis, P. C. E. Moody, E. L. Raven, G. C. K. Roberts, Redox-Linked Domain Movements in the Catalytic Cycle of Cytochrome P450 Reductase. *Structure* **21**, 1581–1589 (2013).

80. J. B. Hopkins, R. E. Gillilan, S. Skou, BioXTAS RAW: improvements to a free open-source program for small-angle X-ray scattering data reduction and analysis. *J Appl Cryst* **50**, 1545–1553 (2017).

81. C. E. Aitken, R. A. Marshall, J. D. Puglisi, An Oxygen Scavenging System for Improvement of Dye Stability in Single-Molecule Fluorescence Experiments. *Biophys J* **94**, 1826–1835 (2008).

82. A. Cheng, C. Negro, J. F. Bruhn, W. J. Rice, S. Dallakyan, E. T. Eng, D. G. Waterman, C. S. Potter, B. Carragher, Leginon: New features and applications. *Protein Sci* **30**, 136–150 (2021).

83. G. Pintilie, W. Chiu, Comparison of Segger and other methods for segmentation and rigid-body docking of molecular components in cryo-EM density maps. *Biopolymers* **97**, 742–760 (2012).

84. J. Abramson, J. Adler, J. Dunger, R. Evans, T. Green, A. Pritzel, O. Ronneberger, L. Willmore, A. J. Ballard, J. Bambrick, S. W. Bodenstein, D. A. Evans, C.-C. Hung, M. O'Neill, D. Reiman, K. Tunyasuvunakool, Z. Wu, A. Žemgulytė, E. Arvaniti, C. Beattie, O. Bertolli, A. Bridgland, A. Cherepanov, M. Congreve, A. I. Cowen-Rivers, A. Cowie, M. Figurnov, F. B. Fuchs, H. Gladman, R. Jain, Y. A. Khan, C. M. R. Low, K. Perlin, A. Potapenko, P. Savy, S. Singh, A. Stecula, A. Thillaisundaram, C. Tong, S. Yakneen, E. D. Zhong, M. Zielinski, A. Žídek, V. Bapst, P. Kohli, M. Jaderberg, D. Hassabis, J. M. Jumper, Accurate structure prediction of biomolecular interactions with AlphaFold 3. *Nature* **630**, 493–500 (2024).

85. P. Emsley, K. Cowtan, Coot: model-building tools for molecular graphics. *Acta Crystallogr D Biol Crystallogr* **60**, 2126–32 (2004).

86. T. I. Croll, ISOLDE: a physically realistic environment for model building into low-resolution electron-density maps. *Acta Cryst D* **74**, 519–530 (2018).

87. (IUCr) Real-space refinement in PHENIX for cryo-EM and crystallography. https://journals.iucr.org/d/issues/2018/06/00/ic5103/index.html.

88. F. P. Guengerich, M. V. Martin, C. D. Sohl, Q. Cheng, Measurement of cytochrome P450 and NADPH–cytochrome P450 reductase. *Nat Protoc* **4**, 10.1038/nprot.2009.121 (2009).

89. Z. A. Maschmann, T. K. Chua, S. Chandrasekaran, H. Ibáñez, B. R. Crane, Redox properties and PAS domain structure of the Escherichia coli energy sensor Aer indicate a multistate sensing mechanism. *J Biol Chem* **298**, 102598 (2022).

90. S. L. Christgen, S. M. Becker, D. F. Becker, Methods for determining the reduction potentials of flavin enzymes. *Methods Enzymol* **620**, 1–25 (2019).

91. C. Lin, S. Feng, C. C. DeOliveira, B. R. Crane, Cryptochrome-Timeless structure reveals circadian clock timing mechanisms. *Nature* **617**, 194–199 (2023).

92. D. Pan, A. Brockmeyer, F. Mueller, A. Musacchio, T. Bange, Simplified Protocol for Cross-linking Mass Spectrometry Using the MS-Cleavable Cross-linker DSBU with Efficient Cross-link Identification. *Anal. Chem.* **90**, 10990–10999 (2018).

93. I. M. Lagerwaard, P. Albanese, A. Jankevics, R. A. Scheltema, Xlink Mapping and AnalySis (XMAS) - Smooth Integrative Modeling in ChimeraX. bioRxiv [Preprint] (2022). https://doi.org/10.1101/2022.04.21.489026.

Acknowledgements: We thank Angela Picciano for helpful discussions. We thank the National Center for CryoEM Access and Training (NCCAT) and the Cornell Center for Material Science (CCMR) for access to data collection facilities. We thank Yajie Xu and Dr Mariena Silvestry Ramos for assistance in CryoEM training and data collection. We thank the Proteomics and Metabolomics Facility of Cornell University for providing the mass spectrometry data and NIH SIG grant 1S10 OD017992-01 support for the Orbitrap Fusion mass spectrometer. The Center for High-Energy X-ray Sciences at CHESS (CHEXS) is supported by the NSF award DMR-2342336, and the MacCHESS resource is supported by NIGMS award 1-P30-GM124166. All figures were created or formated using Biorender.com.

Funding: This work was supported by grant MCB-2129728 from the National Science Foundation to BRC. **Author contributions:** D.N. and B.R.C. designed research, conducted research, analyzed data and wrote the manuscript. Competing interests: The authors declare that they have no competing interests. Data and materials availability: The cryoEM data and structures are available at the Protein Data Bank with accession codes: 9Q05, 9Q06, 9Q0Y, 9Q0X, and 9Q15. All other data needed to evaluate the conclusions in the paper are present in the paper or the Supplementary Materials.

Figures

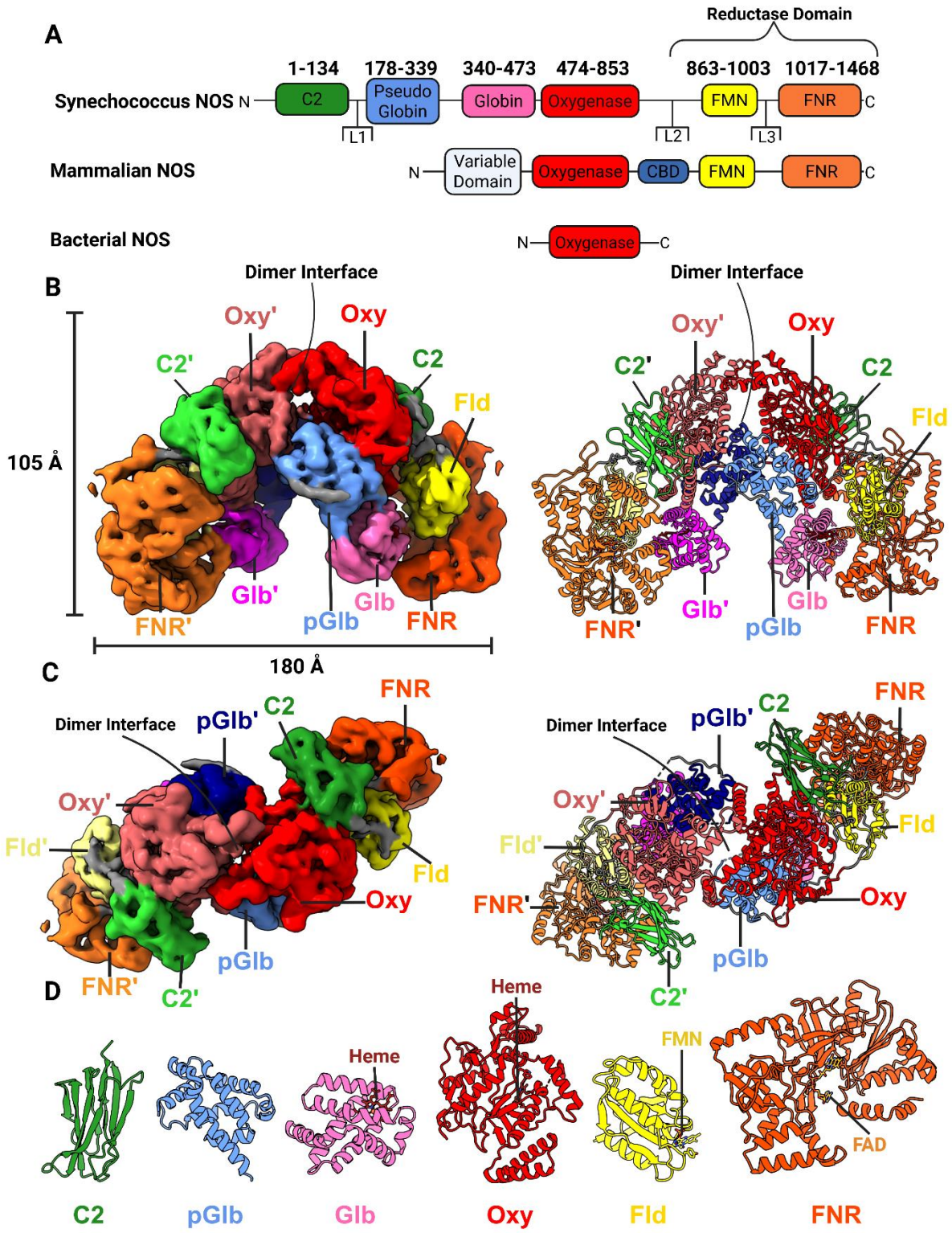
A
Reductase Domain
1-134
178-339
340-473
474-853
863-1003
1017-1468
Synechococcus NOS
N
C2
Pseudo Globin
Globin
Oxygenase
FMN
FNR
C
L1
L2
L3
Mammalian NOS
N
Variable Domain
Oxygenase
CBD
FMN
FNR
C
Bacterial NOS
N
Oxygenase
C
B
Dimer Interface
Oxy'
Oxy
C2'
C2
Fld
105 Å
Glb'
Glb
FNR'
pGlb
FNR
180 Å
C
Dimer Interface
pGlb'
C2
FNR
Oxy'
Fld'
Fld
Oxy
pGlb
FNR'
C2'
D
Heme
FMN
FAD
C2
pGlb
Glb
Oxy
Fld
FNR

907

908 **Figure 1.** Architecture of Ca^{2+}-free locked syNOS (A) Gene architecture of Synechococcus NOS,
909 mammalian NOS and a typical bacterial NOS. Note that some non-cyanobacterial prokaryotic
910 NOSs have auxiliary domains. (B) Sideview of electron density (left, threshold = 0.0298, C2
911 symmetry applied) and corresponding ribbon representation (right) for the locked syNOS
912 homodimer (NOS-Sym). Subunit 1 (right) colored as designated by the gene architecture,
913 Subunit 2 (left) colored as follows: C2' - lime green, pGlb' - navy, Glb' - magenta, Oxy' - indian
914 red, Fld' – pale yellow and FNR' - bright orange . (C) Top view of (B). (D) Individual syNOS
915 domains with cofactors indicated.

916

917

918

919

920

921

922

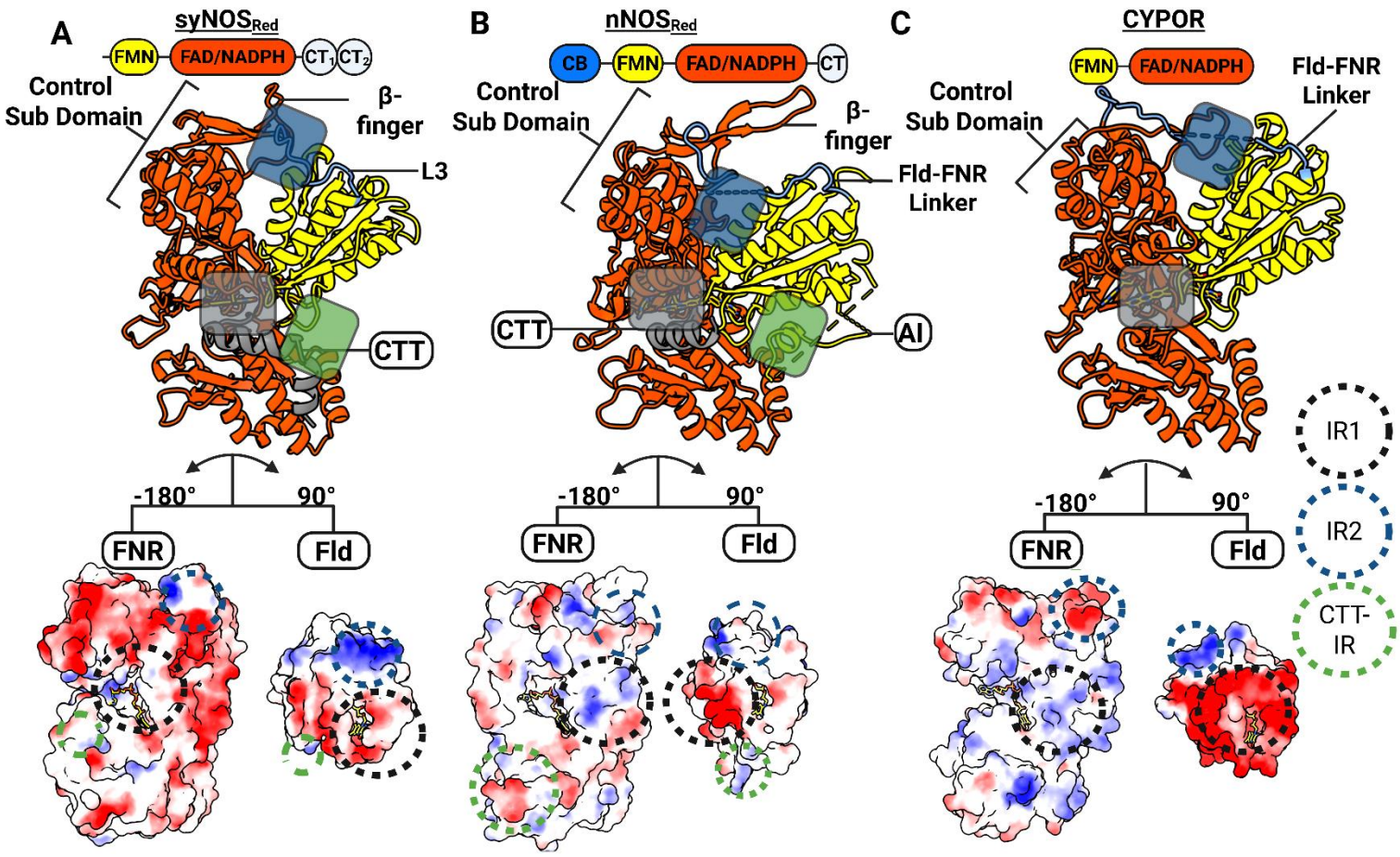

Figure 2. Structural comparison of $syNOS_{Red}$, $nNOS_{Red}$, and CYPOR (A-C). The di-flavin closed conformation is defined by the L3 loop (situated between the Fld and the FNR domain, blue in Fig. 2A, B), the Fld domain, and what we define as Interfacing Region (IR) 1, IR2 and the CTT-IR. Domain architectures (top), the corresponding ribbon diagrams (middle), and key interfaces (lower) mediated by electrostatic interactions for $syNOS_{Red}$ (A), $nNOS_{Red}$ (PDB:1TLL, B) and CYPOR (PDB:1AMO, C) Surfaces are colored by coulombic electrostatic potential (blue – positive; white – neutral; red – negative)) with the Fld and FNR domains separated and rotated to view the interface. Interfacing Regions (IR) 1 (basic-to-acidic patch interactions between the FAD and FMN binding pockets), IR2 (Fld interaction-to-FNR-control region) and CTT-IR (CTT interaction

934 with Fld) are denoted by colored circles in the electrostatic surface representation) and semi-
935 transperant rectangles in ribbons.

936

937

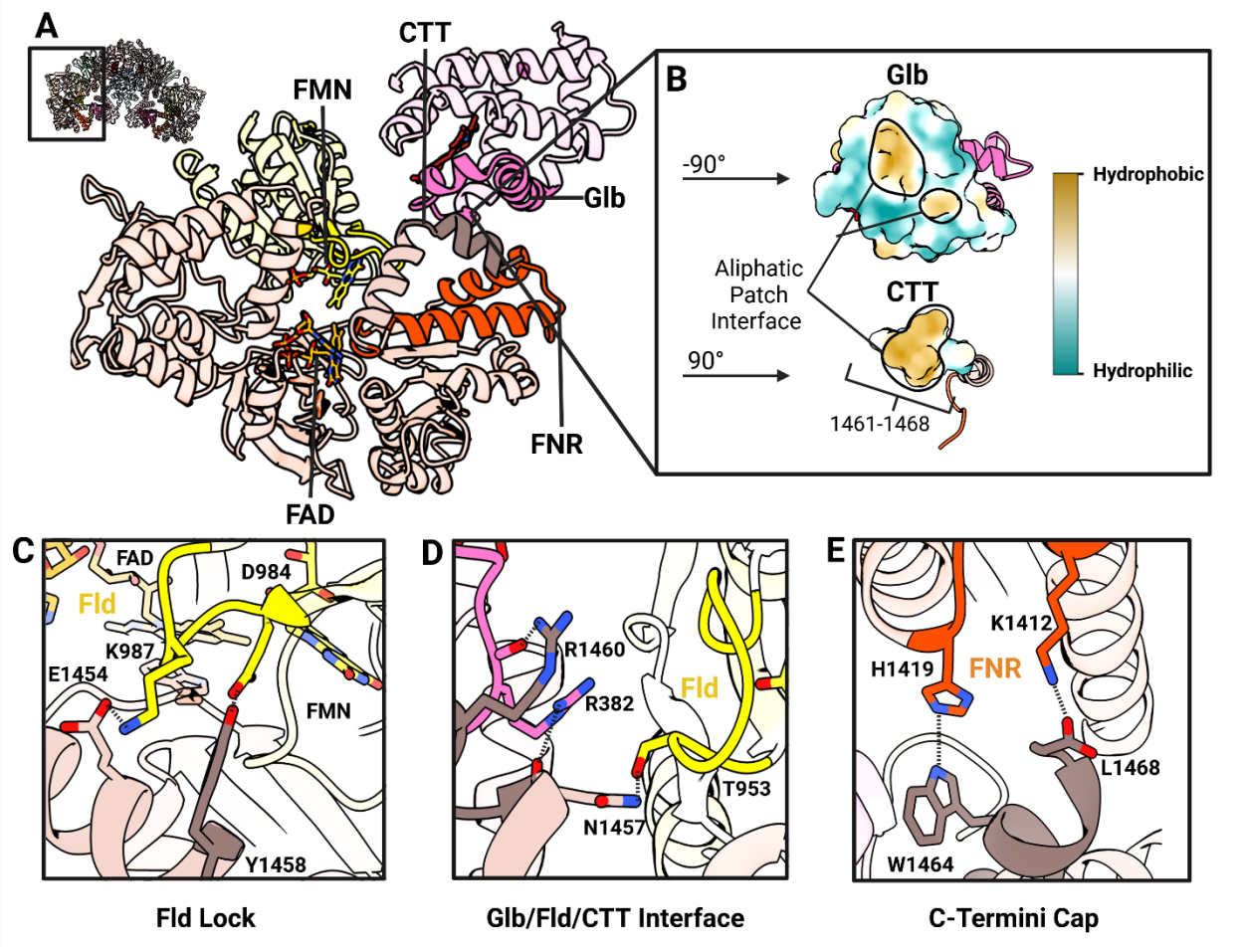

938

939 **Figure 3.** CTT interactions that stabilize the NOS_{Red}-NOS_{Glb} locked state. (A) Ribbon diagram of
940 $syNOS_{Red}$ and $syNOS_{Glb}$ from the boxed region of inactivated $syNOS_{FL}$ (upper left inset) showing
941 key stabilizing interfaces. (B) Aliphatic surface patch between $syNOS_{CTT}$ and $syNOS_{Glb}$ shown by
942 hydrophobicity (yellow) after separating and rotating each domain to view the interface. (C) Fld-
943 to-CTT lock interface mediated by Lys987(Fld)/Glu1454(CTT) salt bridge and
944 Asp984(Fld)/Tyr1458(FNR) and Thr953/Asn1457 hydrogen bonds. (D) Fld-to-Glb interface
945 mediated by Asn1457(CTT)/Thr953(Fld) hydrogen bond, Arg1460(CTT)/Arg382-carbonyl(Glb)
946 hydrogen bond and Asn1457-carbonyl(CTT)/arg382(Glb) hydrogen bond. (E) C-Terminal cap

947 interface mediated by Trp1419(CTT)/His1419(FNR) hydrogen bond and a Leu1468-
948 Carboxyl(CTT)/Lys1412 salt bridge.

949

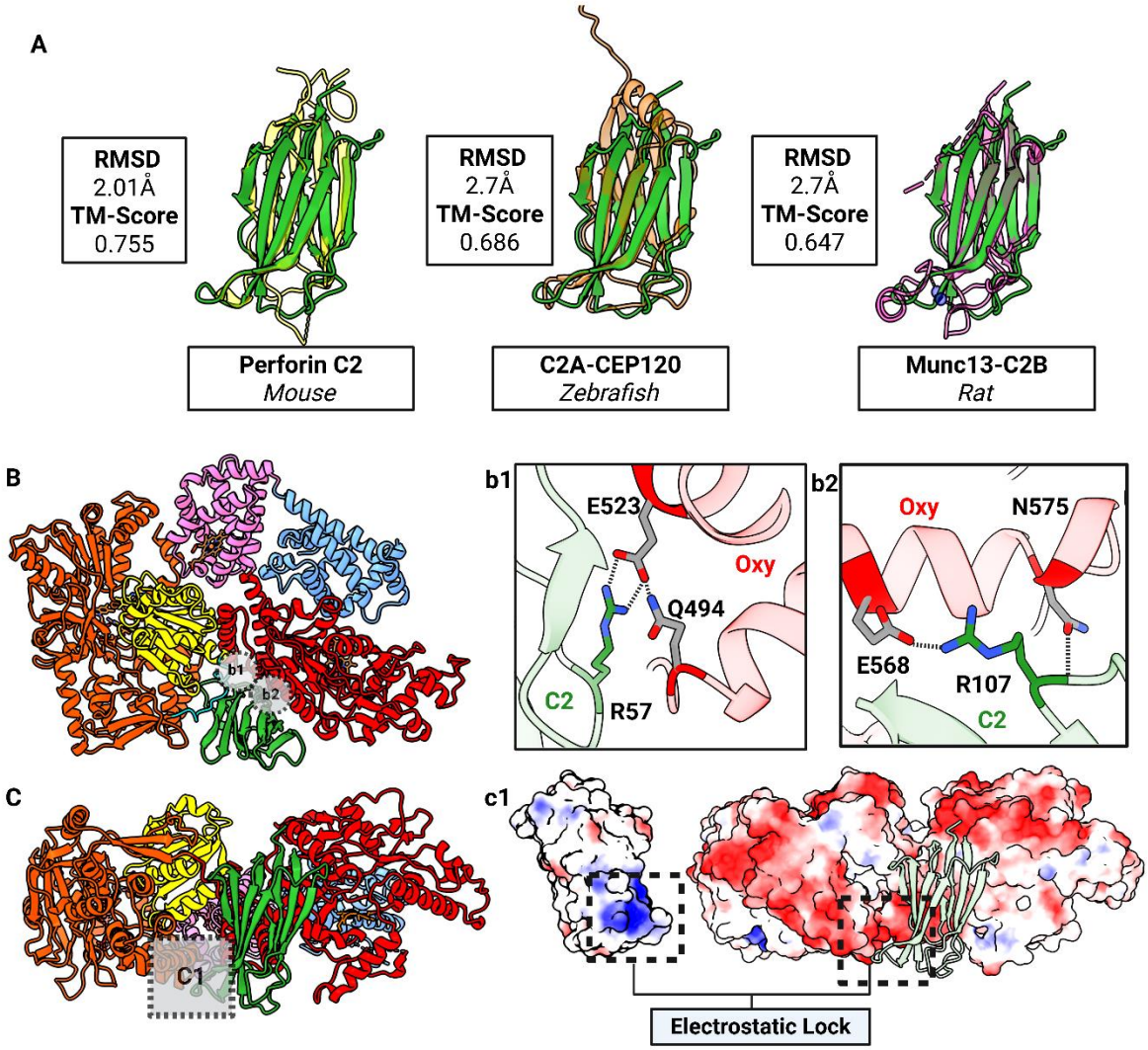

950

951 **Figure 4.** syNOS$_{C2}$ interactions with NOS$_{FNR}$ and NOS$_{Oxy}$. (A) Superimposition of syNOS (C2,
952 green) with Perforin C2 (PDB: 4Y1S, yellow), C2A-CEP120 (PDB:6EWL, orange) and Munc13-C2B
953 (PDB:6NYT, magenta) as labeled, with root mean square deviation (RMSD) of Cα positions
954 (RMSD), and Template Modeling (TM) scores boxed. B) Ribbon diagram of a syNOS subunit,
955 colored by domain with key C2-Oxy interactions shown in insets b1 and b2. b1) Salt bridge
956 between Arg57(C2)/Glu523(Oxy) with Glu523 stabilized by Gln494. b2) Salt bridge between

957 Arg107(C2)/Glu568(Oxy) with the Arg107 amide stabilized by Asn575. (C) Ribbon diagram of a
958 syNOS subunit showing the electrostatic lock interface between $syNOS_{C2}$ and $syNOS_{Oxy}$ in box
959 inset c1. (c1) C2 rotated 90° (left) and FNR (right, orientation as in (C), colored by electrostatic
960 surfaces (colored: blue-positive, white-intermediate and red –negative). C2 (green, ribbons) is
961 also shown in its original position for reference.

962

963

964

965

966

967

968

969

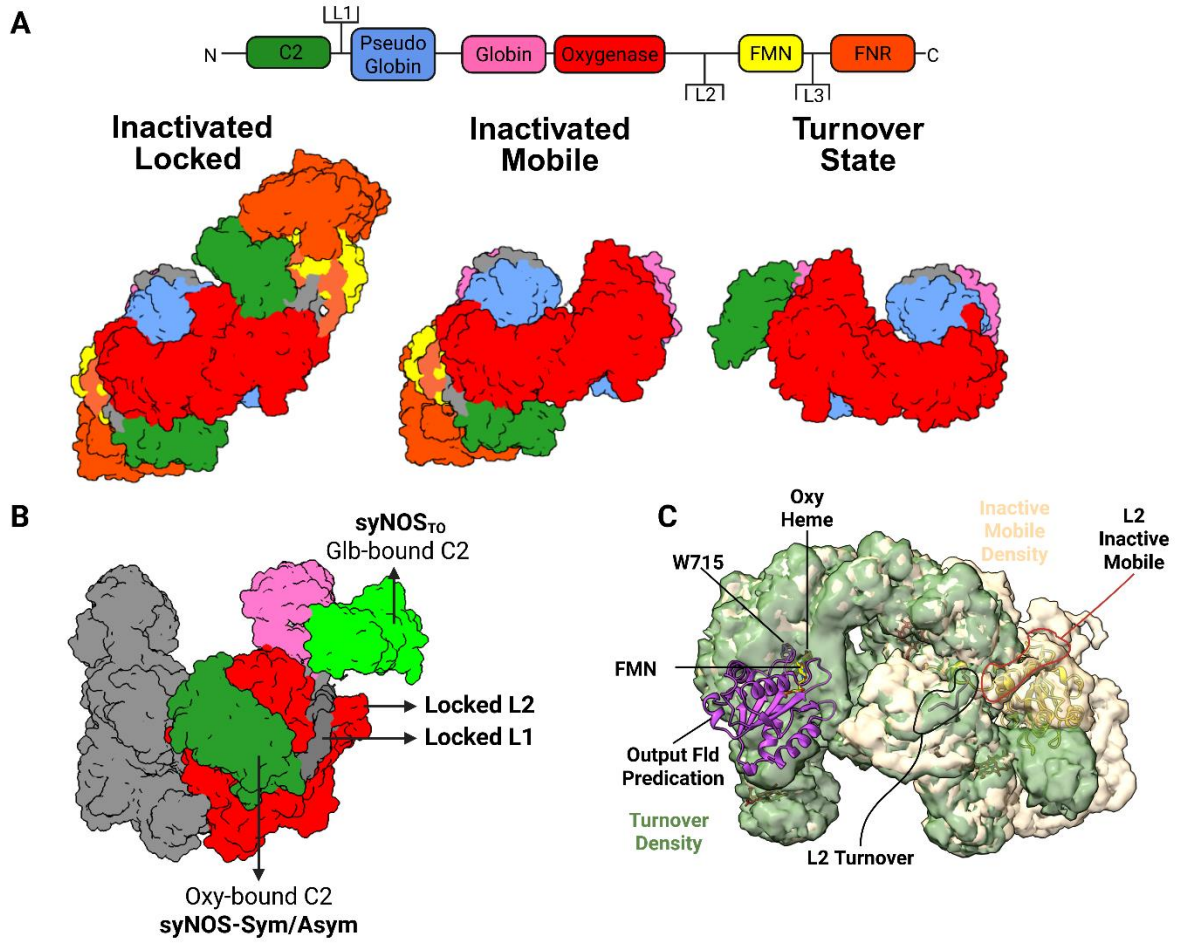

Figure 5. Ca^{2+}-activated C2 mobility. (A) syNOS gene architecture colored by domain, with linkers labeled L1-3(above). Surface representation of three separate syNOS states with relative orientations of the C2 domain. (B) Superimposed surface representations of the turnover state (C2 – lime green) and inactivated states (C2 – forest green, Oxy – red and Glb – hot pink) reveal dramatically different C2 positions. (C) L2 in the turnover state (tan electron density) connects to the Fld (yellow ribbons) but then swivels 135° (green density) from its position in the inactivated state to direct the NOS_{Fld} to the adjacent NOS_{Oxy} subunit (purple ribbons of AlphaFold prediction).

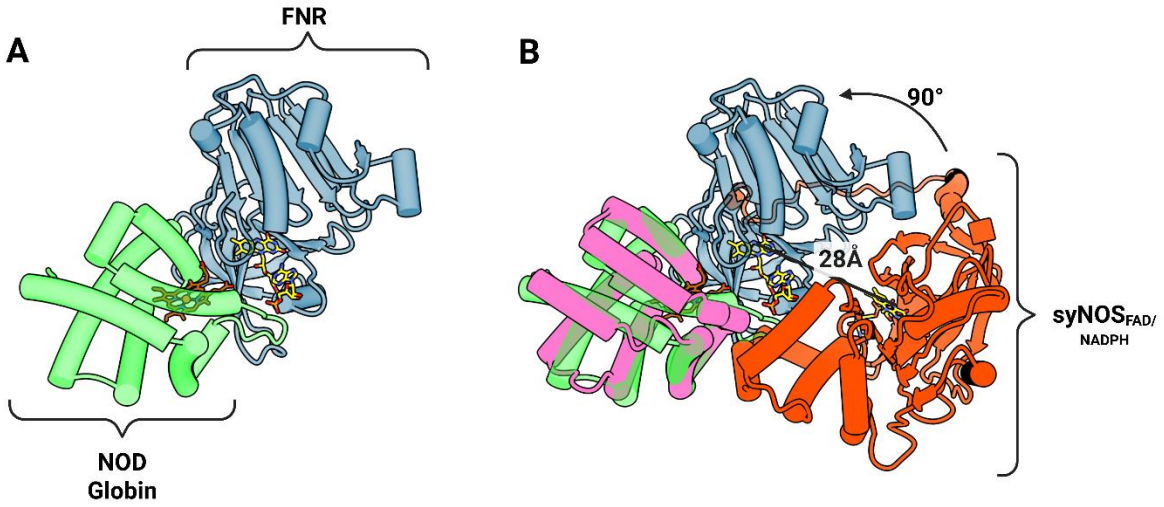

Figure 6. syNOS$_{FNR}$ likely requires a large conformational change to reduce syNOS$_{Glb}$. (A) Cartoon representation of E.*coli* Hmp (PDB: 1GVH) with the NOD domain (lime green) and FNR (metallic blue) domains orientated to show the Heme-to-FAD separation of 17.8 Å. (B) syNOS$_{Glb}$ (purple) and associated syNOS$_{FNR}$ domain (red, control region 1084-1224 not shown) superimposed on the Hmp Glb (green) and associated FNR (blue). SyNOS$_{FNR}$ would need to rotate 90° and translate 28 Å to adopt an equivalent Hmp conformation.

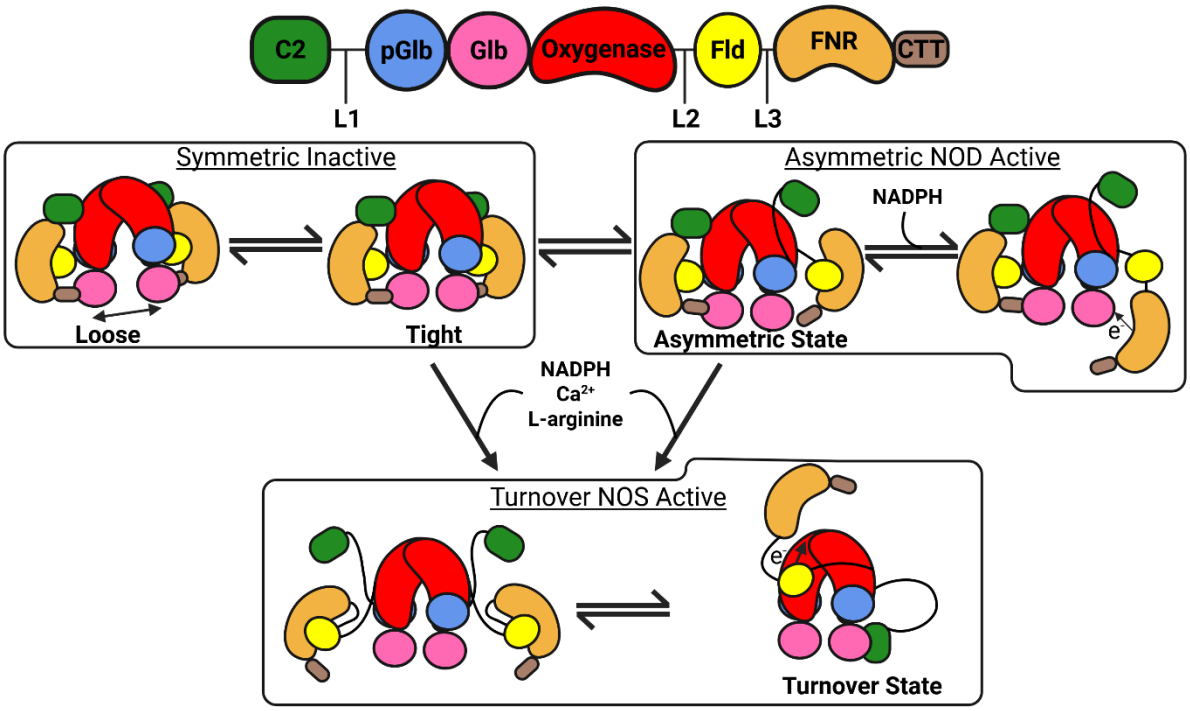

988

989 **Figure 7.** Model for NOS to NOD activity switching in syNOS. In the inactivated locked state
990 $syNOS_{Oxy}$ equilibrates between a loose and tight dimer, the latter stabilized by BH_4. This state
991 can transition into the asymmetric NOD active state which involves a release of a C2 domain
992 from one subunit and increased mobility of NOS_{Fld} and NOS_{FNR}, such that NOS_{FNR} can reduce the
993 $syNOS_{Glb}$ to activate NOD activity. $SyNOS_{Glb}$ reduction coincides with a loosening of the CTT to
994 allow hydride transfer from NADPH to FAD and movement of $syNOS_{FNR}$. In the presence of
995 Ca^{2+}/NADPH/L-arginine syNOS rearranges to facilitate NOS activity. The displacement of $syNOS_{C2}$
996 from NOS_{Oxy} and its binding to NOS_{Glb} relieves constraints on L2 and exposes the Trp715 site
997 such that NOS_{FNR} can relocate to NOSOxy on the opposing subunit and reduce the NOS_{Oxy} heme
998 for NO production.

999

1000

1001

Structure and dynamics of a muti-domain nitric oxide synthase regulated by a C2 domain

Dhruva Nair and Brian R. Crane

Supplementary Movies

Movie S1: 3D Flexible Refinement of syNOS dimer shows a 'breathing' motion

Supplementary Tables

Table S1: Description of datasets, conditions and refined classes.

Table S2: Identified and validated DSBU crosslinks

Table S3: Cryo-EM data collection, refinement, and validation statistics.

Table S4: DNA primers used in the study with the cloning approach.

Table S5: Reduction potentials ($E^{0'}$) for $syNOS_{Glb}$, $syNOS_{Fld}$ and $syNOS_{FNR}$ vs. the Normal Hydrogen Electrode (NHE)

Supplementary Figures

Figure S1: syNOS purification

Figure S2: Dataset 1 processing scheme

Figure S3: Dataset 2 processing scheme

Figure S4: Merged data for NOS-Sym state, boxed class used for 3DVA and 3DFlex

Figure S5: Dataset 3 processing scheme and validation.

Figure S6: Dataset 4 processing scheme and validation

Figure S7: Dataset 5 processing scheme and validation

Figure S8: syNOS linker intertwining

Figure S9: syNOS tight and loose NOS_{Oxy} states

Figure S10: Identified cross-links plotted onto dimer interface Oxy+pGlb and the syNOS FNR+CTT

Figure S11: Phylogenetic sequence clustering in the context of $syNOS_{Red}$.

Figure S12: C-terminal tail (CTT) sequence alignment of syNOS, mNOSs and diatom NOS.

Figure S13: Density validation of key interactions

Figure S14: SEC-SAXS of syNOS and variants.=

Figure S15: Steady state cytochrome c reductase activities of WT syNOS and variants

Figure S16: Flavin reduction by NADPH

Figure S17: Isothermal calorimetric titration of Ca^{2+} with $syNOS_{C2}$

Figure S18: syNOS NOD activity and heme reduction rates

Figure S19: Output state predicted by AlphaFold3

Supplemental Movies

Movie S1. 3D Variability analysis of one subunit of the syNOS asymmetric dimer showing the breathing motion of NOS_{Red} as a unit relative to motion about the NOS_{Oxy} interface.

Supplementary Tables

Dataset	Conditions	Class 1	Class 2
1 **2**	GFB1	Symmetric Dimer (NOS-Sym)	Asymmetric Dimer (NOS-Asym)
3	GFB1 + 1mM Ca^{2+}/ 1mM L-arg / BH_4*	Asymmetric Dimer (NOS-Asym)	Turnover (NOS-TO_L)
4	GFB1 + 1mM Ca^{2+}/ 1mM L-arg / BH_4*	Asymmetric Dimer (NOS-Asym)	Turnover (NOS-TO_T)
5	GFB1 + 1mM Ca^{2+}/1mM L-arg/ BH_4* / 1mM NADPH	Monomer (NOS-Mon)	none

GFB1: 25 mM HEPES (pH 7.5), 150 mM NaCl, 1 mM TCEP, 10% glycerol and 10 µM BH_4.

*****Additional 25 µM BH_4 was supplemented.

Table S1. Description of datasets, conditions and refined classes.

1047

1048

1049

1050

Inactive				
Residue 1	**Residue 2**	**Intra Cα- Cα**	**Inter Cα- Cα**	**XlinkX Score**
FNR - FNR				
1111	1017	**8**	143	124
1366	1447(CTT)	**20**	117	118
1053	1463(CTT)	**40**	121	75
1366	1053(CTT)	**21**	138	52
Interdomain				
191(pGlb)	538(Oxy)	**17**	**24**	78

Turnover				
Residue 1	**Residue 2**	**Intra Cα- Cα**	**Inter Cα- Cα**	**XlinkX Score**
FNR-FNR				
1019	1111	**6**	149	222
1111	1017	**8**	143	86
Interdomain				
196(pGlb)	538(Oxy)	**16**	**31**	97
191(pGlb)	538(Oxy)	**17**	**24**	78
470(Glb)	481(Oxy)	**17**	57	61
473(Glb)	481(Oxy)	**12**	58	50
196(pGlb)	481(Oxy)	**24**	44	48
413(Glb)	592(Oxy)	**19**	79	45
1017(FNR/L3)	994(Fld)	**23**	120	41
470(Glb)	538(Oxy)	40	55	41

1051 **Table S2.** Identified and validated DSBU crosslinks. Reasonable distances based on the cryo-EM

1052 structures are bolded and underlined. PDB:9Q15 was used to estimate distances.

Dataset		Ca2+/L-Arginine			Ca^{2+}/L-Arginine/NADPH
State	**Symmetric Dimer**	**Asymmetric**	**Turnover**	**Asymmetric (Composite)**	**Monomer**
Data Collection and Processing					
Microscope	Arctica		Krios		Krios
Voltage (keV)	200		300		300
Detector	K3		Gatan K3		Falcon4EC
Nominal magnification	63,000		105,000		105,000
Data Acquisition Software	Serial EM		Leginon		Leginon
Electron dose (e–/Å2)	50		50.5		44.95
Pixel Size (Å) (binned)	1.31		0.422(0.844)		0.7304
Defocus range (μm)	0.5-2		0.4-2.1		0.4-2.2
Number of movies (#)	1214 + 4055		5019		9036
Number of particles	131,000	70,944	61,553	70,944	45,964
Symmetry imposed	C2	C1	C1	C1	C1
Resolution (Å)	3.95	3.16	3.69	3.16	3.09
FSC threshold	0.143	0.143	0.143	0.143	0.143
Refinement					
Initial model used	PDB 9Q15	PDB 9Q15	PDB 9Q15	Alphafold	PDB 9Q15
Non-hydrogen atoms	22712	16319	11268	16319	11404
Protein residues	2796	2001	1358	2001	1398
Ligand(#)	Heme(4) FAD(2) FMN(2)	Heme(2) FAD(1) FMN(1)	Heme(4)	Heme(4) FAD(1) FMN(1)	Heme(2) FAD(1) FMN(1) NADPH(1)
RMS Deviation					
Bond lengths (Å)	0.02	0.005	0.003	0.003	0.003
Bond angles (°)	1.55	0.55	0.574	0.485	0.519
MolProbity score	1.54	1.58	1.5	1.74	1.54
Clashscore	2.18	3.49	4.65	4.66	4.93
Poor rotamers (%)	2.08	1.63	0.93	1.8	0.91
Ramachandran Favored (%)	95.1	96.0	96.1	95.5	96.0
Ramachandran Allowed (%)	4.6	3.9	3.7	4.3	3.8
Ramachandran Disallowed (%)	0.3	0.2	0.2	0.2	0.2
Fit to map (CCmask)	0.8	0.79	0.75	0.81	0.82
EMDB (maps)	EMD-72088	EMD-72110	EMD-72109	EMD-72104, EMD-72105,EMD-72116	EMD-72087
PDB (model)	9Q06	9Q0Y	9Q0X	9Q15	9Q05

Table S3. Cryo-EM data collection, refinement, and validation statistics.

Primer Name	Primer	Cloning Approach
pet28_twin_strep_syNOS_fwd	tcgagcaccaccaccacc	Gibson/NEB HiFi
pet28_twin_strep_syNOS_rev	catatgtcctccggattggaagtac	Gibson/NEB HiFi
syNOS_fwd	tccaatccggaggacatatgatgcttgtcaacgactctc	Gibson/NEB HiFi
syNOS_rev	gtggtggtggtggtgctcgagctacaagttggctagcc	Gibson/NEB HiFi
Hptg_fwd_PAYC_mcs1	TAATGCTTAAGTCGAACAG	Gibson/NEB HiFi
Hptg_rev_PAYC_mcs1	GGTATATCTCCTTATTAAAGTTAAAC	Gibson/NEB HiFi
Hptg_fwd	CTTTAATAAGGAGATATACCATGAAAGGACAAGAAACTCGTG	Gibson/NEB HiFi
Hptg_rev	TCTGTTCGACTTAAGCATTATCAGGAAACCAGCAGCTG	Gibson/NEB HiFi
gapa_fwd_pAYC_mcs2	TAATTAACCTAGGCTGCTG	Gibson/NEB HiFi
gapa_rev_pAYC_mcs2	ATGTATATCTCCTTCTTATACTTAAC	Gibson/NEB HiFi
gapa_fwd	TATAAGAAGGAGATATACATATGACTATCAAAGTAGGTATCAAC	Gibson/NEB HiFi
gapa_rev	GCAGCAGCCTAGGTTAATTATTATTTGGAGATGTGAGC	Gibson/NEB HiFi
pet28_tws_delc2_fwd	ctcgagcaccaccaccac	Gibson/NEB HiFi
pet28_tws_delc2rev	catatgtcctccggattggaag	Gibson/NEB HiFi
syNOSdelc2_178_1468_fwd	tccaatccggaggacatatgacctactcagaagccgtc	Gibson/NEB HiFi
syNOSdelc2_178_1468_fwd	tggtggtggtggtgctcgagctacaagttggctagccatttttc	Gibson/NEB HiFi
pet28_tws_delctt_fwd	tagctcgagcaccaccac	Gibson/NEB HiFi
pet28_tws_delctt_rev	catatgtcctccggattggaag	Gibson/NEB HiFi
syNOS_delctt1_1_1440_fwd	tccaatccggaggacatatgatgcttgtcaacgactctc	Gibson/NEB HiFi
syNOS_delctt1_1_1440_fwd	tggtggtggtgctcgagctagtagttgtctttctccacttg	Gibson/NEB HiFi
syNOS_K1412E_fwd	GCAAATTGCTgaaACAGAAGGAG	KLD
syNOS_K1412E_rev	ATAAATACCTCAAACACATTG	KLD
syNOS_T953A_fwd	GATCGGCAGCgcgGTCTATGAAC	KLD
syNOS_T953A_rev	CCTAGTACGGAATAGTTGAG	KLD
syNOS_K987A_fwd	CGACGAAATCgcgGGACAAGCCG	KLD
syNOS_K987A_rev	CCTTTATGTAGGGGAAC	KLD

Table S4. Primers used in the study with the cloning approach (left).

Domain	Couple	Potential (mV)	n	Calibrating dye (mV)
Globin (337-467)	Fe^{3+}/Fe^{2+}	-250 ± 20	1	safranin T (-289, 12.5μM)
Fld (856-1027)	ox/hq	-173 ± 3	2	cresyl violet (-177.0, 60 μM)
FNR (1027-1468)	ox/hq	-290 ± 13	2	safranin T (-289, 12.5 μM)

Table S5. Reduction potentials ($E^{0'}$) for $syNOS_{Glb}$, $syNOS_{Fld}$ and $syNOS_{FNR}$ vs. the Normal Hydrogen Electrode (NHE). For $syNOS_{Glb}$ the single electron reduction (n_e=1) from Fe^{3+} to Fe^{2+} was measured whereas for the flavin-containing domains a midpoint potential for the 2-electron reduction (n_e=2) from oxidized (ox) to hydroquinone (hq) was measured as no spectral signature for the semiquinone was apparent in the titrations. (n = 3 for all measurements)

Supplementary Figures

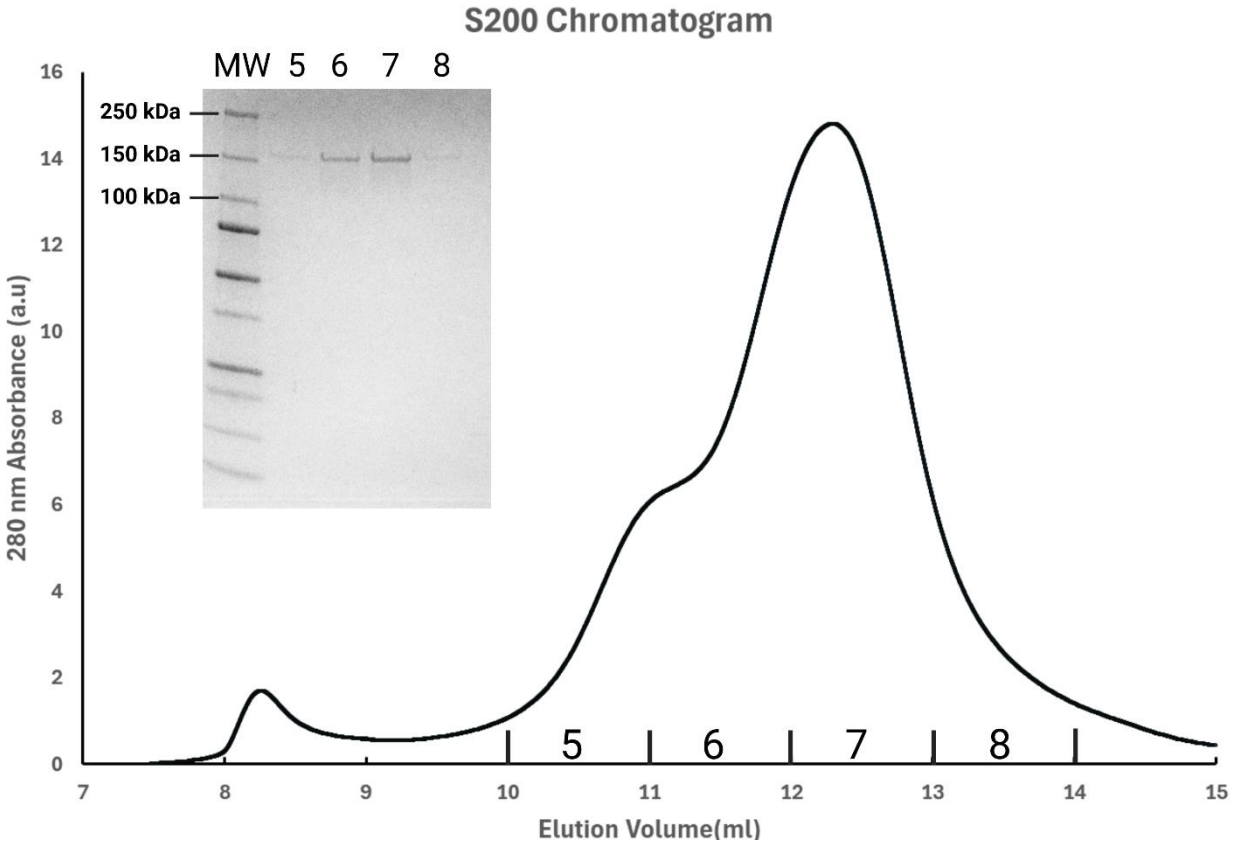

Figure S1. syNOS Purification. Representative chromatogram from a Superdex 200 increase 10/30 size exclusion chromatography column with an arrow denoting the syNOS dimer peak. The inset corresponds to a Coomassie blue stained 4-12% SDS-PAGE gel of fractions 5,6,7 and 8.

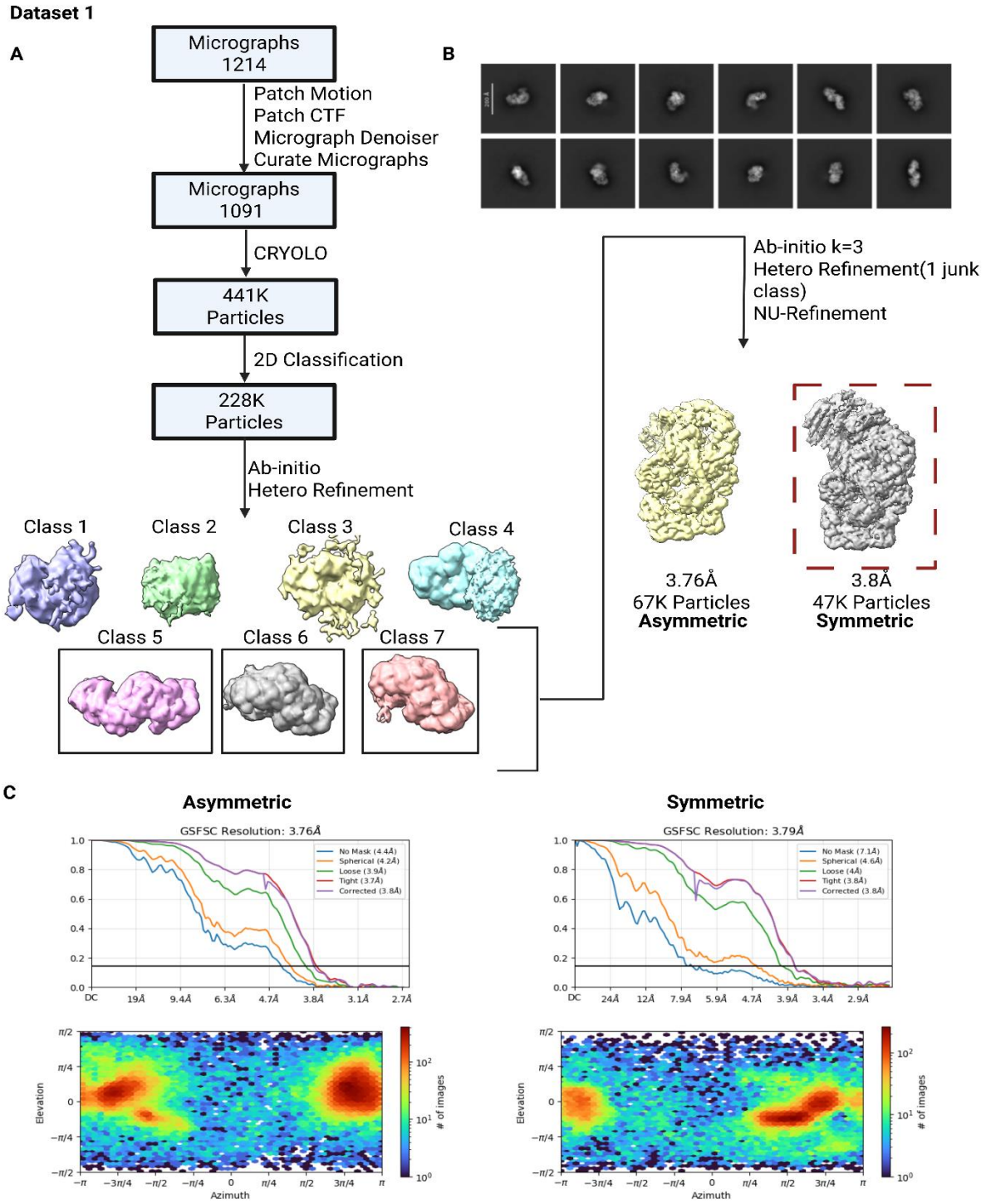

Figure S2. Dataset 1 processing scheme. (A) CryoEM processing workflow for dataset 1: syNOS ligand free. NOS-Sym class used for 3DVA and 3DFlex boxed (dashed-red). (B) Representative

1075 2D Classes. CTF, contrast transfer function; NU, non-uniform refinement. (C) Overall Particle and

1076 Gold-standard Fourier Shell Correlation (GSFSC) curves for NOS-Asym and NOS-Sym.

1077

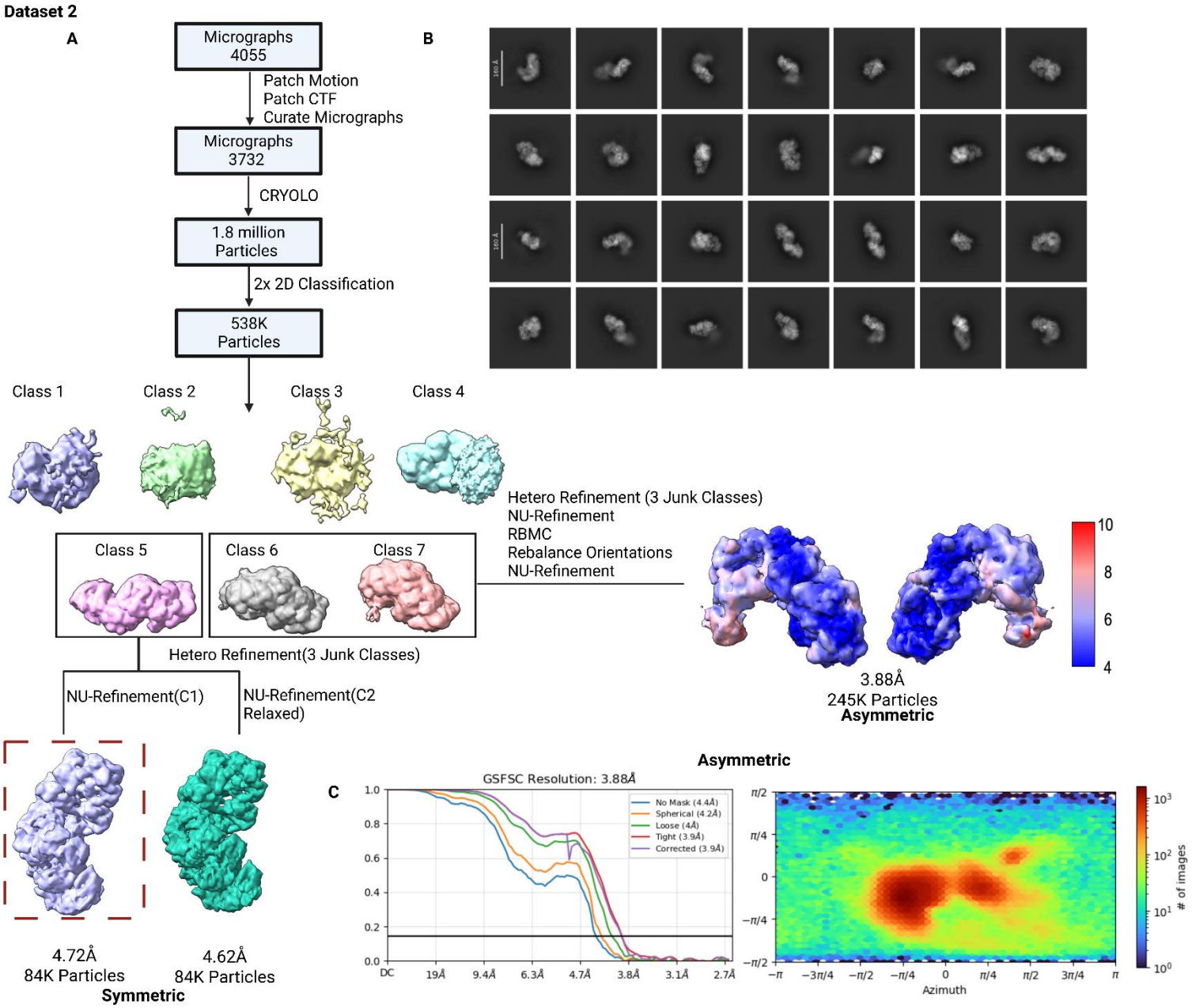

1078

1079 **Figure S3.** Dataset 2 processing scheme. (A) CryoEM processing workflow for dataset 2: syNOS
1080 ligand free. NOS-Sym class used for 3DVA and 3DFlex boxed (dashed-red). (B) Representative 2D
1081 Classes. (C) GSFSC curves and positional distribution of particles.

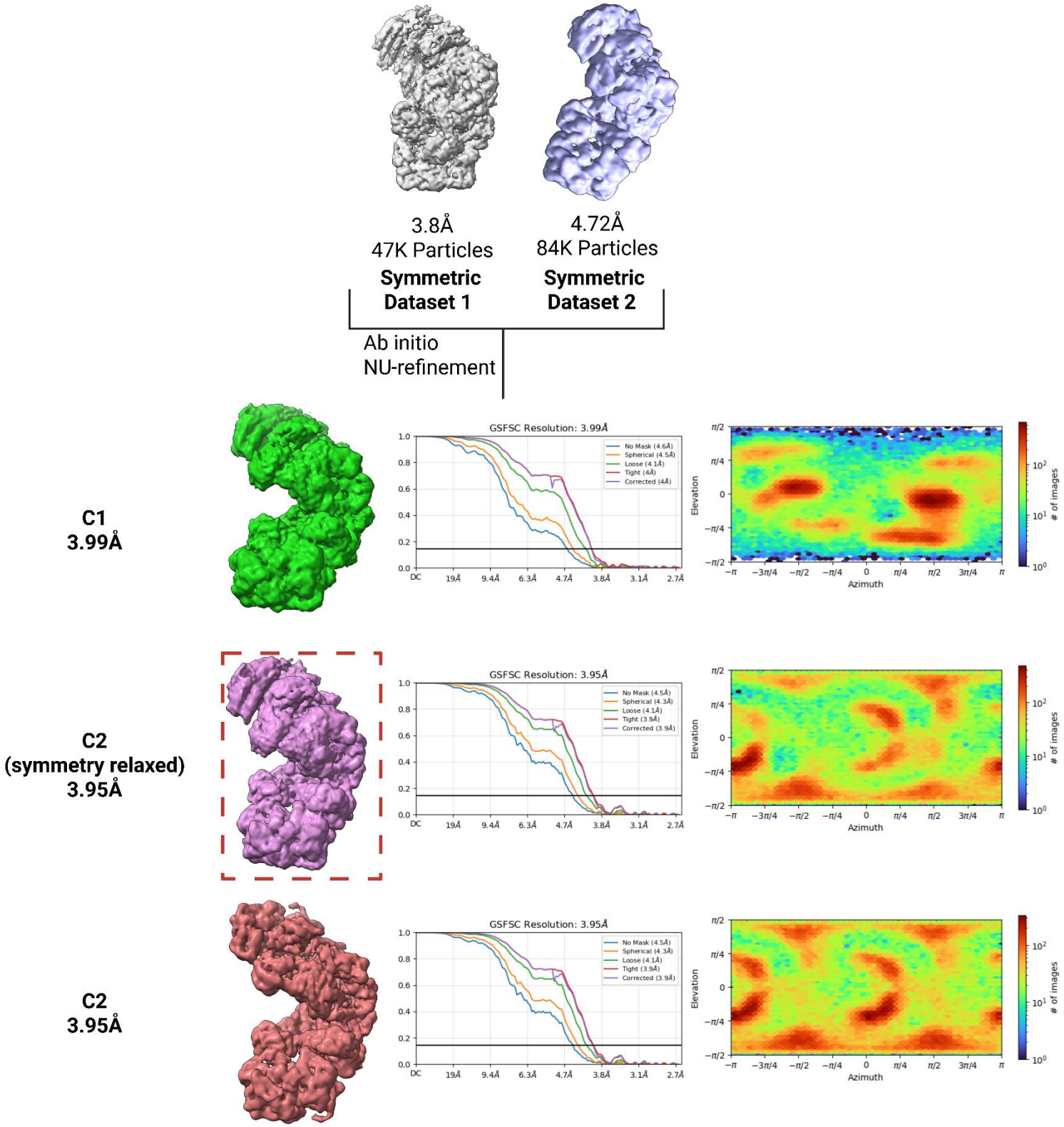

1082 **Figure S4.** Merged data for NOS-Sym state, boxed class used for 3DVA and 3DFlex.

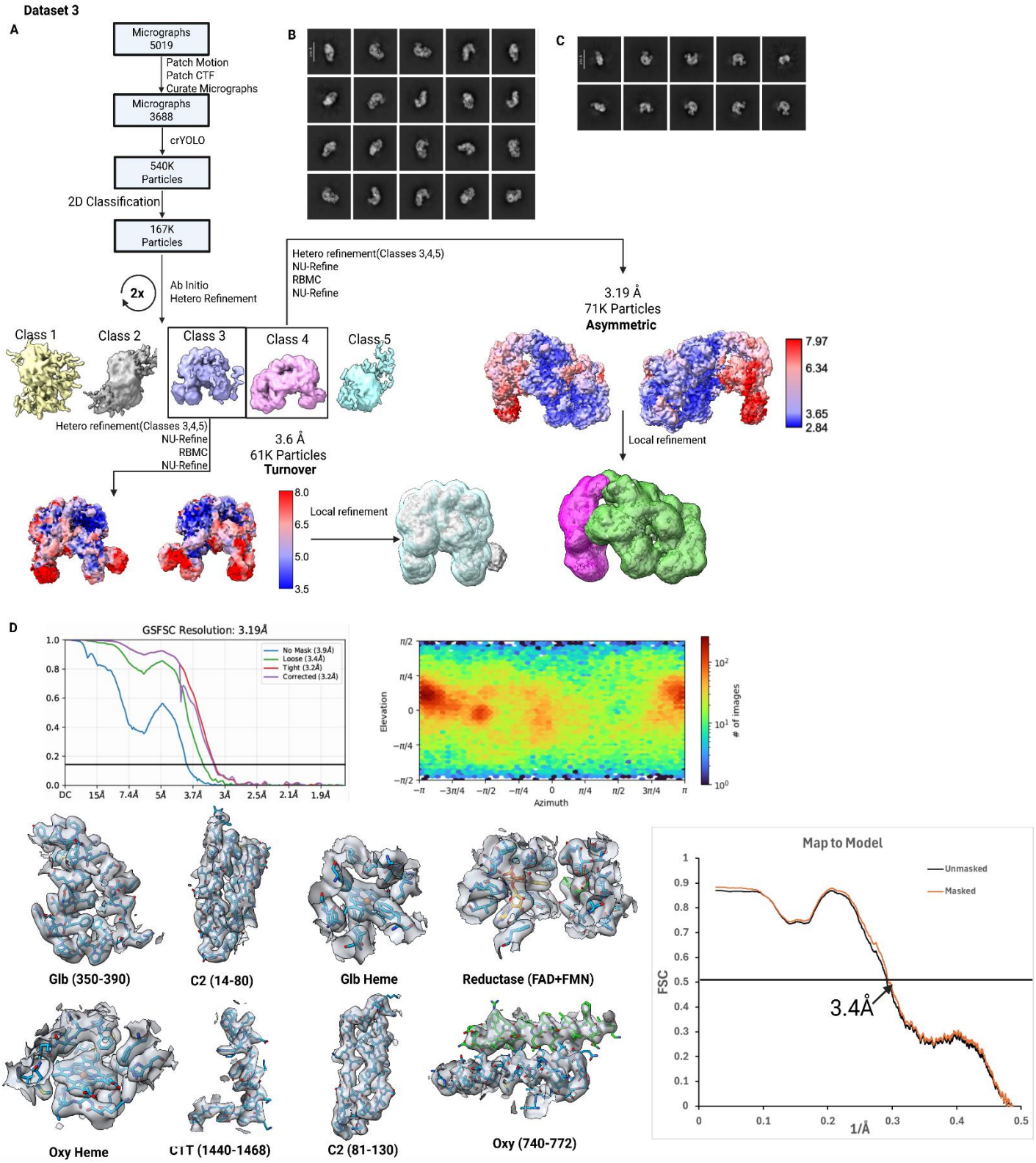

Figure S5. Dataset 3 processing scheme and validation. (A) CryoEM processing workflow for dataset 3: syNOS in the presence of Ca^{2+}/L-arginine (B) Representative 2D Classes for NOS-Asym

1085 state (C) Representative 2D classes for NOS turnover state (NOS-TO_L) (D) Asymmetric states
1086 GSFSC curves, orientation validation, model density fit and map to model Fourier Shell
1087 Correlation (FSC).

1088

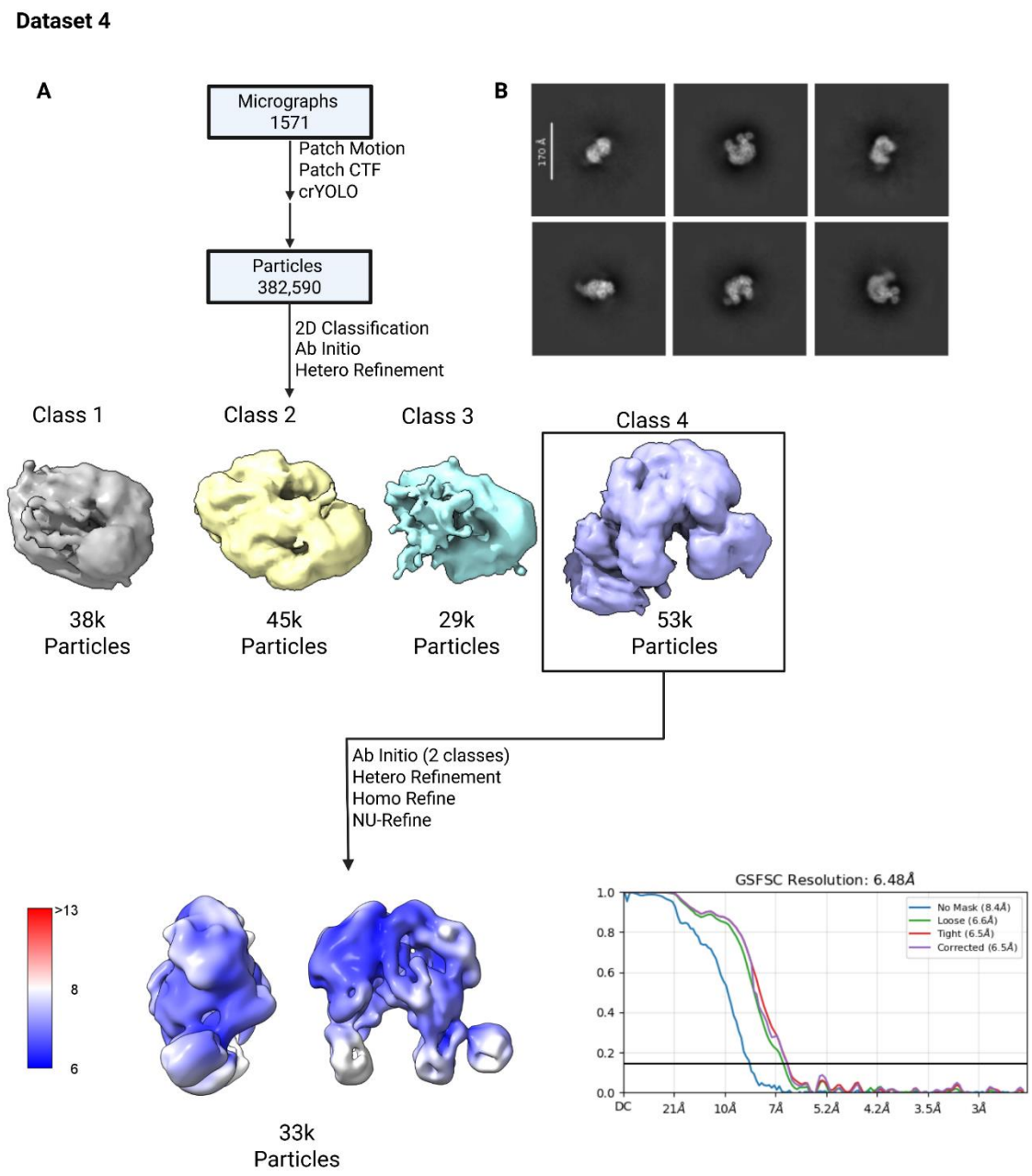

1089

1090 **Figure S6.** Dataset 4 processing scheme and validation. (A) CryoEM processing workflow for

1091 dataset 4, syNOS with NADPH/Ca^{2+} including GSFSC curves. (B) Representative 2D classes for

1092 NOS-TO_T.

Dataset 5

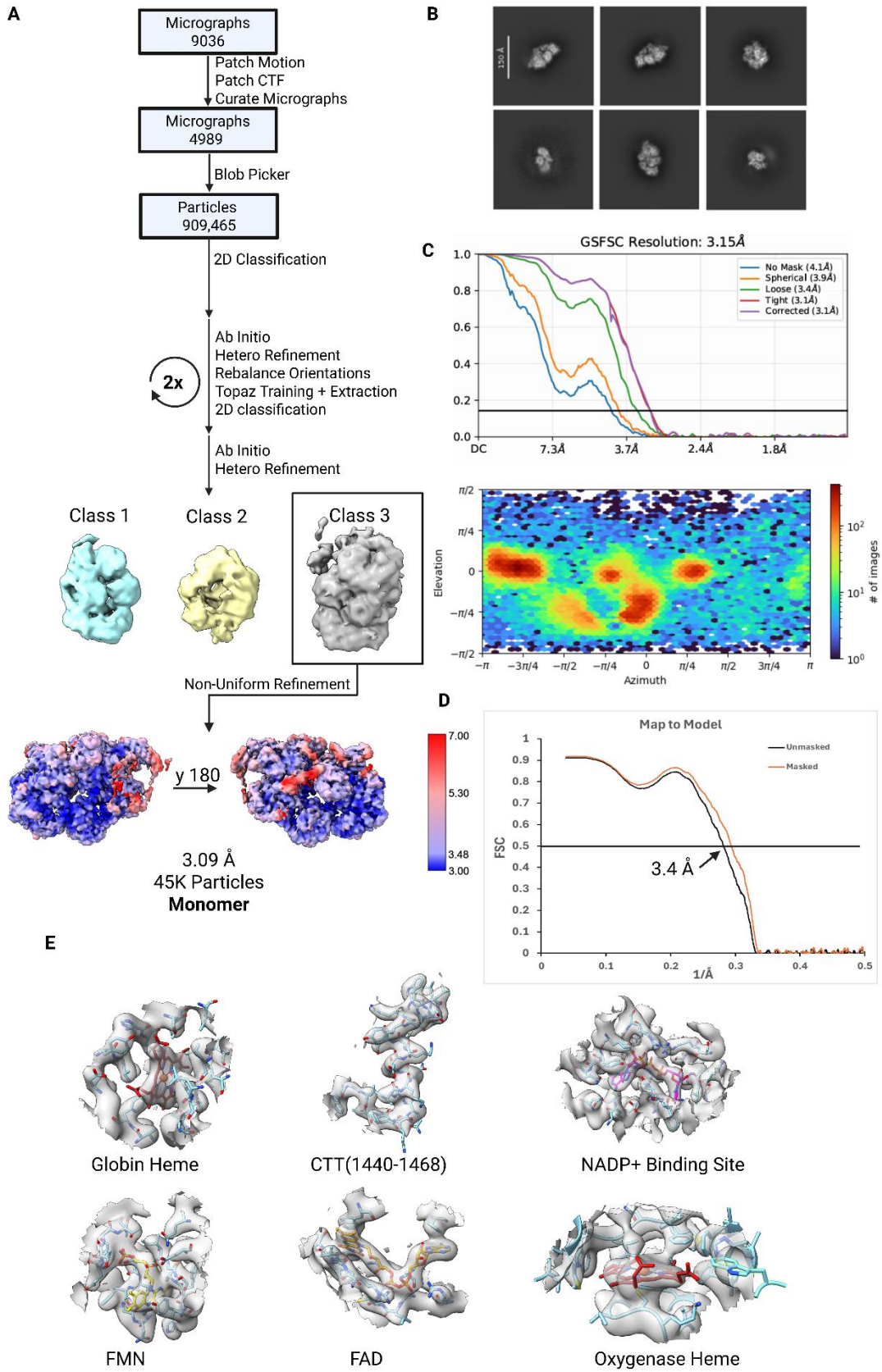

1093

1094 **Figure S7**. Dataset 5 processing scheme and validation. (A) CryoEM processing workflow for
1095 dataset 5: syNOS with L-arginine, NADPH/Ca^{2+}/NADPH (B) Representative 2D classes for NOS-
1096 Mon. (C) GSFSC curves, orientation validation and (D) Map to Model FSC. (E) Density fit of
1097 model in map.

1098

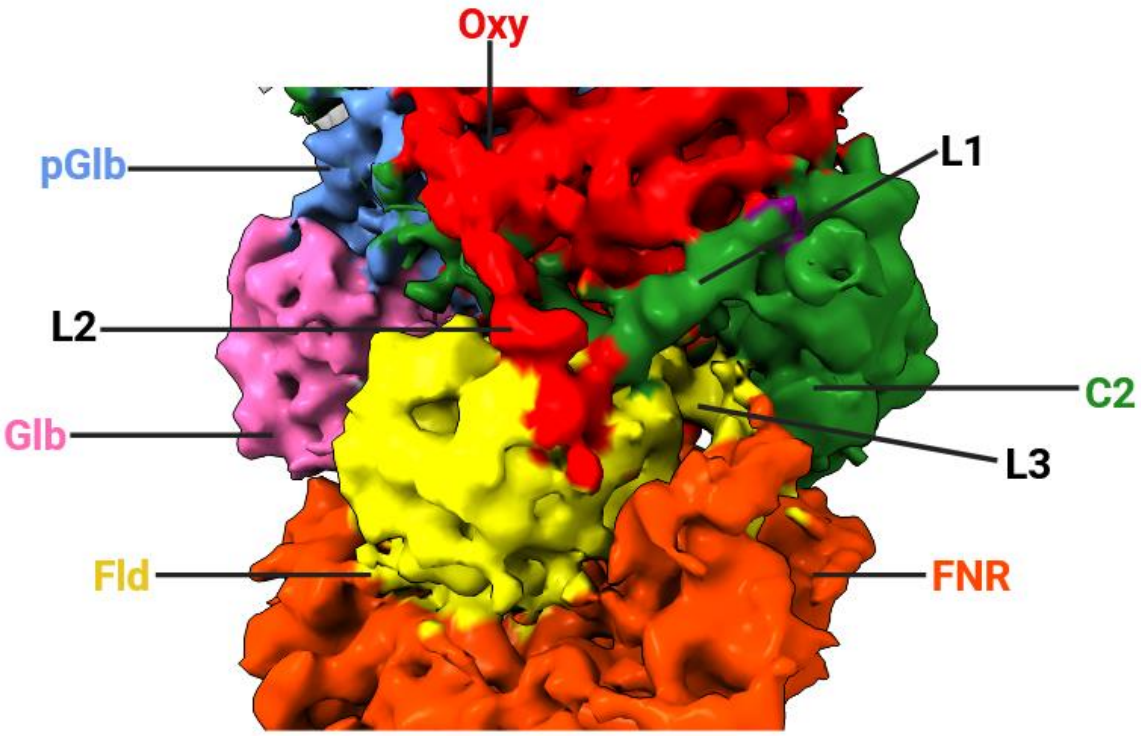

1099

1100 **Figure S8.** SyNOS linker intertwining. Intermediate resolution homodimer cryoEM density with
1101 all three linkers colored the same as their preceding domains. Note how L1 threads beneath L2
1102 and on top of L3. Movement of the C2 domain (green) will release the Fld module for NOS_{Oxy}
1103 reduction.

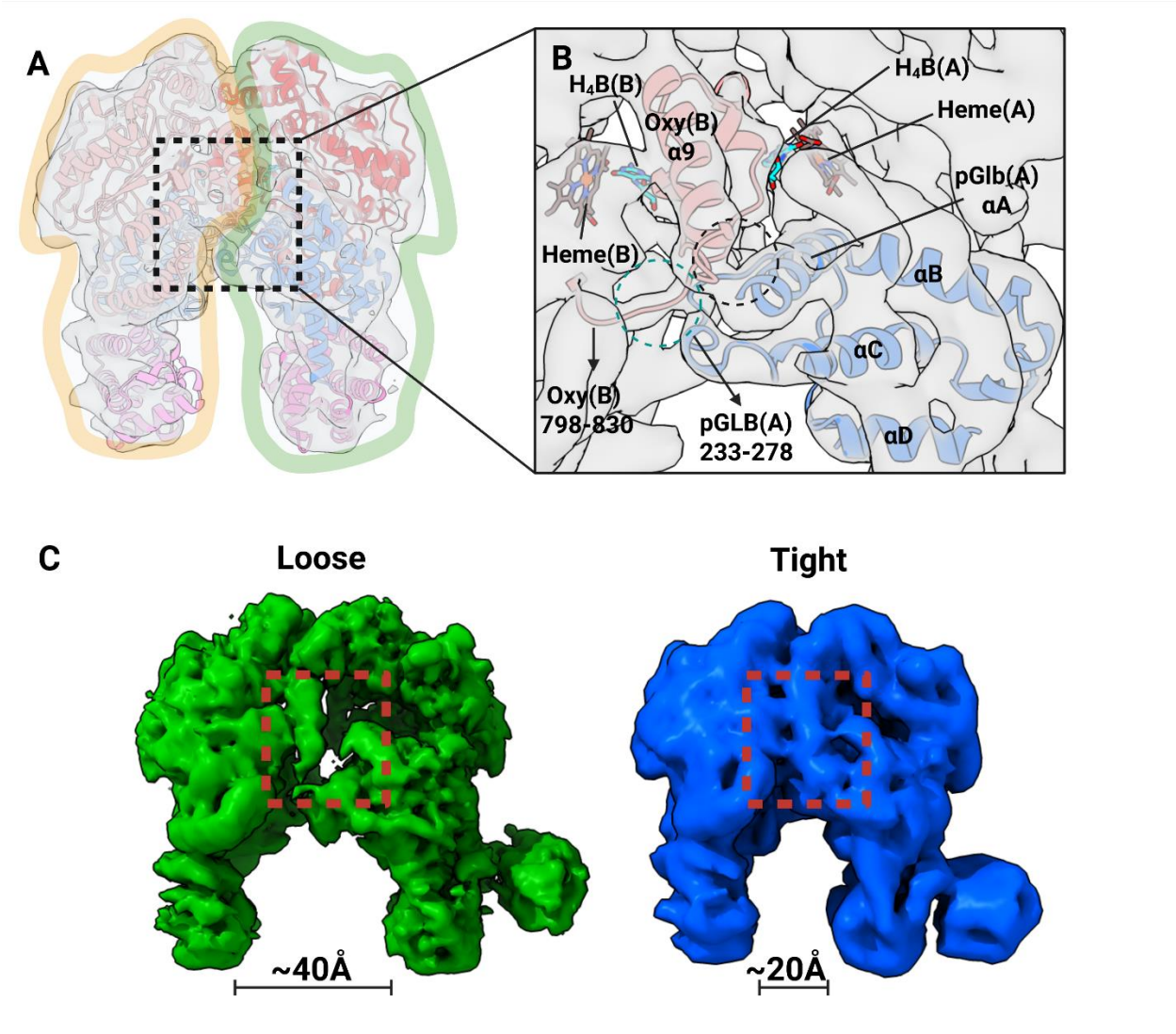

Figure S9. SyNOS tight and loose NOS_{Oxy} states. (A) syNOS cryoEM density (dataset 4) with the NOS_{Oxy} dimer interface outlined (orange and green) to show each subunit. (B) Close up of the dimeric interface showing the close association of NOS_{Oxy} α9 to an intersubunit pGlb C/D loop. Although at lower resolution, strong electron density for the core the NOS-TO_T interface includes the helical lariats and BH_4. (C) Loose (green) and tight (blue) NOS_{Oxy} dimers differ by a large 20 Å breathing motion normal to the dimer interface that also affects the positioning of the C2 domain (lower right peripheral electron density).

A

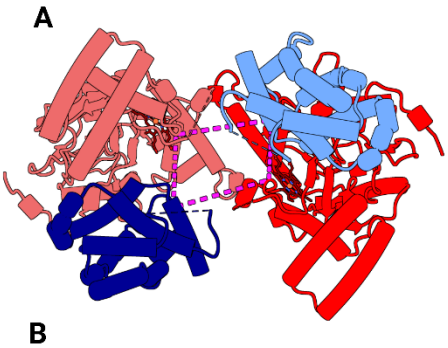

Inactive Dimer Interface

Residue 1	Residue 2	Intra Cα- Cα	Inter Cα- Cα	XlinkX Score
191(pGlb)	538(Oxy)	**17**	**24**	78

B

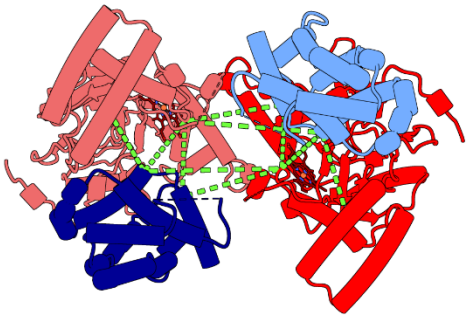

Turnover Dimer Interface

Residue 1	Residue 2	Intra Cα- Cα	Inter Cα- Cα	XlinkX Score
196(pGlb)	538(Oxy)	**16**	**31**	97
191(pGlb)	538(Oxy)	**17**	**24**	78
196(pGlb)	481(Oxy)	**24**	**44**	48

C

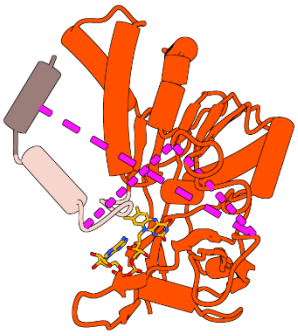

Inactive CTT

Residue 1	Residue 2	Intra Cα- Cα	Inter Cα- Cα	XlinkX Score
1366	1447(CTT)	**20**	117	118
1053	1463(CTT)	**40**	121	75
1366	1053(CTT)	**21**	138	52

Figure S10. DSBU crosslinks plotted onto the dimer interface of syNOS Oxy + pGlb and the syNOS FNR + CTT. (A) syNOS inactive dimer interface, subunit 1 Oxy (red) + pGlb (blue) and subunit 2 Oxy (bright red) + pGlb (navy), with magenta crosslinks corresponding to table (left). (B) syNOS inactive dimer interface, protomer 1 Oxy (red) + pGlb (blue) and subunit 2 Oxy (bright red) + pGlb (navy), with green crosslinks corresponding to table (left). (C) syNOS inactive CTT with magenta crosslinks corresponding to table (left). Crosslinks within range based on the structures are underlined and bolded.

1125

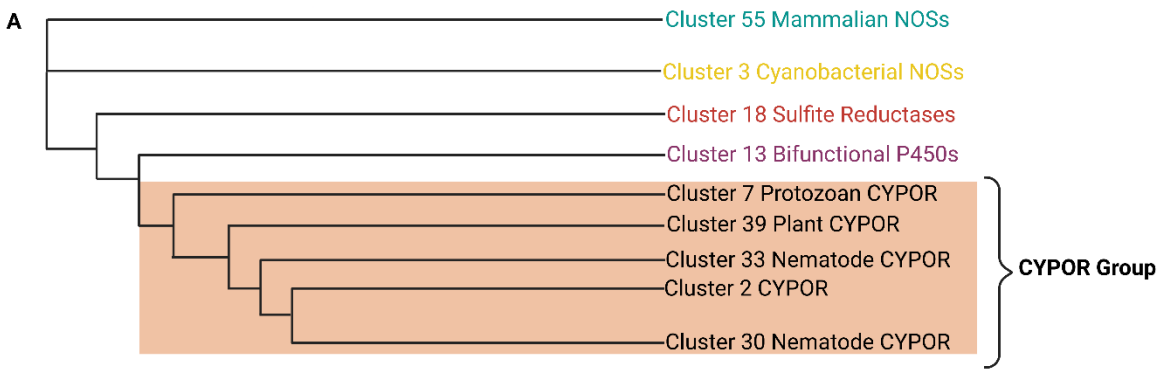

B

Cluster ID	Average Sequance Length	Standard Deviation of Sequence Length	Sequence Count
2	678	63	2521
39	702	49	1588
55	1117	103	278
3	1479	118	94
13	976	174	63
58	700	17	49
30	1126	283	47
7	638	35	45
18	601	74	44
33	652	36	44

1126 **Figure S11.** Phylogenetic sequence clustering in the context of syNOS$_{Red}$(residues 853-1468).

1127 Representative clusters were subjected to PhyML with clusters above 40 sequences represented

1128 in the tree. (B) Cluster composition by sequence length and count.

1129

1130

1131 **Figure S12.** C-terminal tail (CTT) sequence alignment of syNOS, mNOSs and diatom NOS.

1132

1133

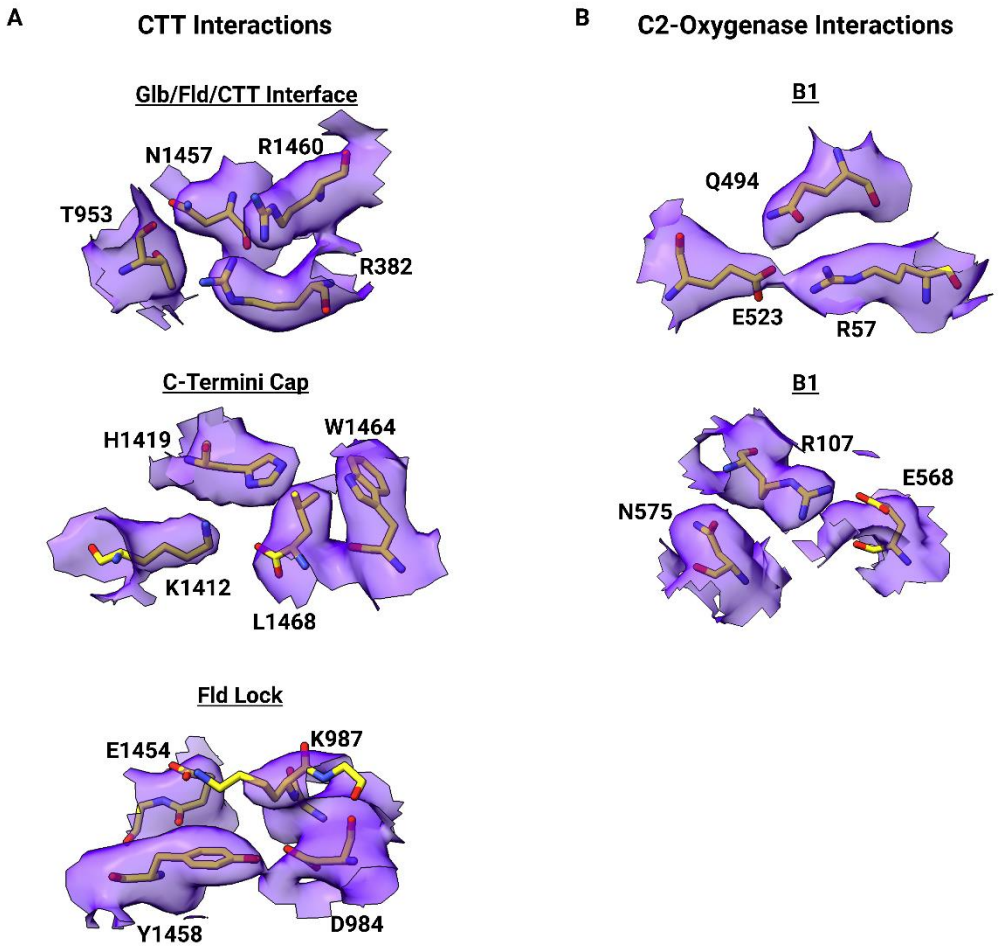

Figure S13. Cryo-EM density validation of key interactions. (A) Density fit of syNOS-Asym (9Q15), key interactions shown in Fig 3 C-E (B) Density fit of syNOS-Asym (9Q15), key interactions shown in Fig 4. B1-B2.

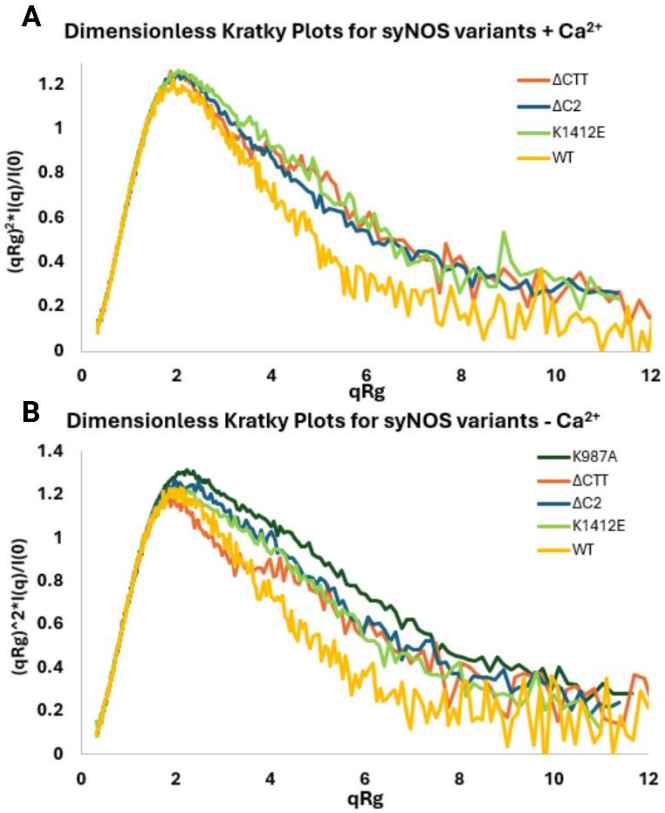

C

Sample	Rg [Guinier] (Å)	MW(Vc)	MW(Vp)
Predicted WT Dimer	55.59	-	-
Predicted WT Monomer	38.81	-	-
WT Ca^{2+}	52.83 ± 0.44	277.8	316.8
ΔC2 Ca^{2+}	56.89 ± 0.29	317.9	366.9
ΔCTT Ca^{2+}	62.71 ± 0.37	237.9	288.6
K1412E Ca^{2+}	57.16 ± 0.3	222	284
WT EGTA	52.83 ± 0.44	234.7	280.2
ΔC2 EGTA	57.34 ± 0.3	222.7	272.2
ΔCTT EGTA	61.18 ± 0.55	313.3	360
K1412E EGTA	55.28 ± 0.24	221.4	258.2
K987A EGTA	58.79 ± 0.37	213.6	266.7

Figure S14. SEC-SAXS of syNOS and variants. (A) Dimensionless Kratky plots, binned by 4 qRg values, for samples in the presence and absence of Ca^{2+}. (B) Table of predicted and experientially characterized radius of gyrations (Rgs) and molecular weights calculated either by volumes of correlation (V_C) or Porod volumes (V_P). (Samples were measured once)

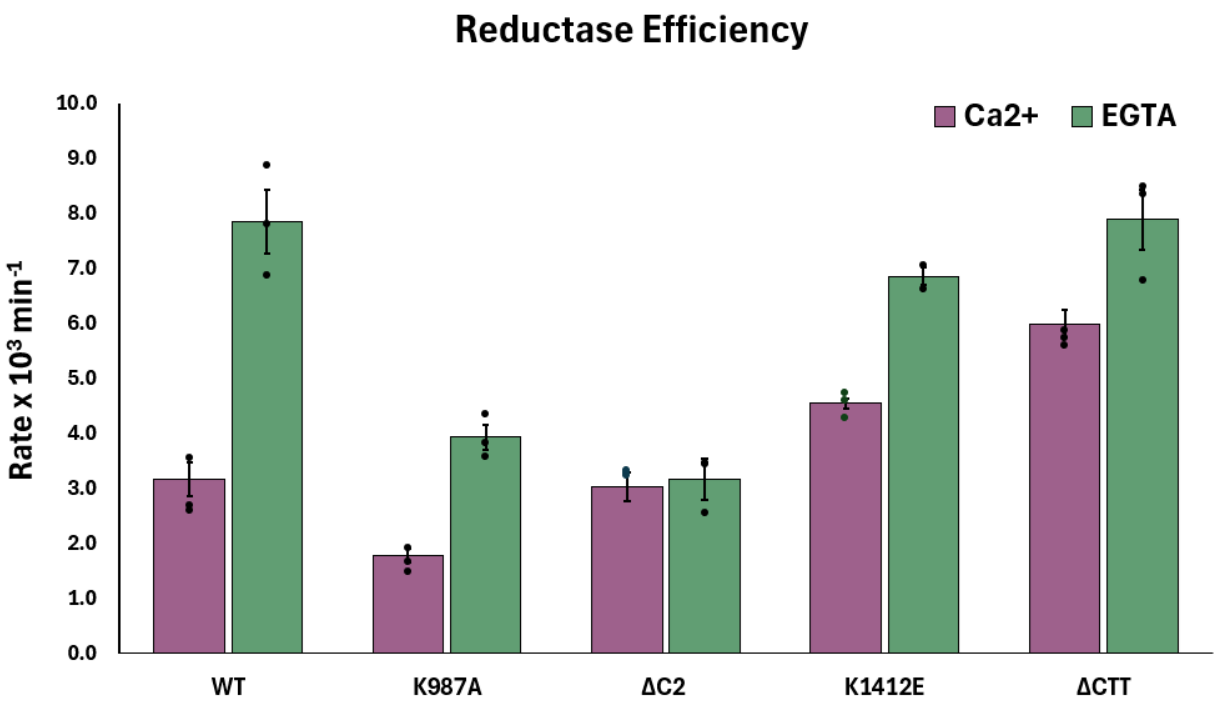

1147

1148 **Figure S15.** Steady state cytochrome c reductase activities of WT syNOS and variants expressed
1149 as turnover numbers (Cc reduced (NOS subunit)$^{-1}$ min^{-1}) with standard errors shown as error
1150 bars (see Methods). Statistical comparisons between groups were performed with a 2-way
1151 ANOVA with post hoc analysis using Tukey's multiple comparisons test. Significant differences
1152 are indicated as follows: ns (not significant), * ($p \leq 0.05$), ** ($p \leq 0.01$), *** ($p \leq 0.001$), **** ($p \leq$
1153 0.0001)..Ca:WT vs. Ca:K987A (ns); Ca:WT vs. Ca:ΔC2 (ns); Ca:WT vs. Ca:K1412E (ns); Ca:WT vs.
1154 Ca:ΔCTT (ns); Ca:WT vs. EGTA:WT (****) ; Ca:WT vs. EGTA:K987A (ns); Ca:WT vs. EGTA:ΔC2 (ns);
1155 Ca:WT vs. EGTA:K1412E (****); Ca:WT vs. EGTA:ΔCTT (****) ;Ca:K987A vs. Ca:ΔC2 (ns);
1156 Ca:K987A vs. Ca:K1412E (***); Ca:K987A vs. Ca:ΔCTT (****); Ca:K987A vs. EGTA:WT (**);
1157 Ca:K987A vs. EGTA:K987A (**); Ca:K987A vs. EGTA:ΔC2 (ns); Ca:K987A vs. EGTA:K1412E (****);
1158 Ca:K987A vs. EGTA:ΔCTT (****); Ca:ΔC2 vs. Ca:K1412E (ns); Ca:ΔC2 vs. Ca:ΔCTT (**); Ca:ΔC2 vs.
1159 EGTA:WT (****); Ca:ΔC2 vs. EGTA:K987A (ns); Ca:ΔC2 vs. EGTA:ΔC2 (ns); Ca:ΔC2 vs.
1160 EGTA:K1412E (****); Ca:ΔC2 vs. EGTA:ΔCTT (****);Ca:K1412E vs. Ca:ΔCTT (ns); Ca:K1412E vs.
1161 EGTA:WT (****); Ca:K1412E vs. EGTA:K987A (ns); Ca:K1412E vs. EGTA:ΔC2 (ns); Ca:K1412E vs.
1162 EGTA:K1412E (**); Ca:K1412E vs. EGTA:ΔCTT (****); Ca:ΔCTT vs. EGTA:WT (**); Ca:ΔCTT vs.
1163 EGTA:K987A (*); Ca:ΔCTT vs. EGTA:ΔC2 (***); Ca:ΔCTT vs. EGTA:K1412E (ns); Ca:ΔCTT vs.

EGTA:ΔCTT (**); EGTA:WT vs. EGTA:K987A (****); EGTA:WT vs. EGTA:ΔC2 (****); EGTA:WT vs. EGTA:K1412E (ns); EGTA:WT vs. EGTA:ΔCTT (ns); EGTA:K987A vs. EGTA:ΔC2 (ns); EGTA:K987A vs. EGTA:K1412E (***); EGTA:K987A vs. EGTA:ΔCTT (***); EGTA:ΔC2 vs. EGTA:K1412E (****); EGTA:ΔC2 vs. EGTA:ΔCTT (****); EGTA:K1412E vs. EGTA:ΔCTT (ns). (n=3, except for K1412E +EGTA; n = 2).

A

Reductase	λ_{obs}	A_1 (%)	k_{obs1} (s^{-1})	A_2 (%)	k_{obs2} (s^{-1})	A_3 (%)	K_{obs3} (s^{-1})	
$syNOS_{Red}$(-Ca^{2+})	450	89	178 (± 0.78)	11	4.12 (± 0.03)	-	-	This study
$syNOS_{FL}$(-Ca^{2+})	450	63	2.38 (± 0.03)	37	0.004 (± 0.001)	-	-	This study
$nNOS_{Red}$(-CAM)	458	28	57 (± 1)	52	5.2 (± 0.1)	20	570 (± 41)	Craig et al.[17]
$nNOS_{Red}$(+CAM)	458	44	608 (± 66)	56	86 (± 2)	-	-	Craig et al.[17]
CYPOR	450	90	42 (± 4)	10	3.8 (± 0.5)	-	-	Hamdane et al.[68]

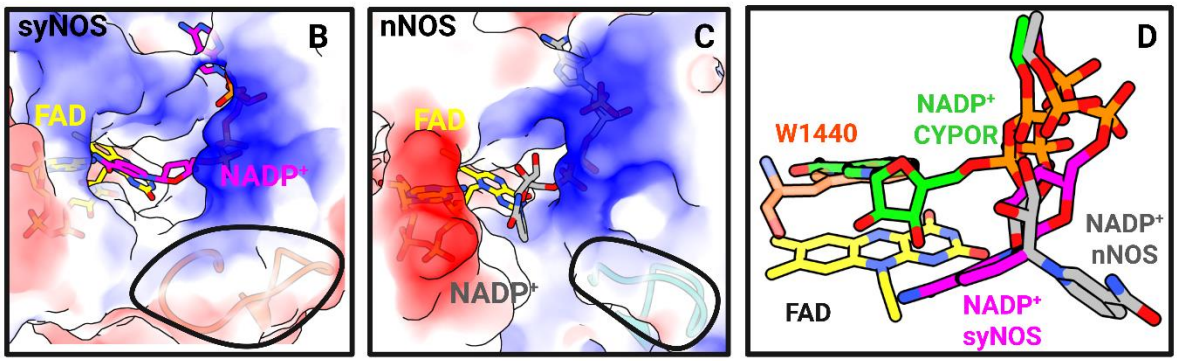

Figure S16. Flavin reduction by NADPH. (A) Table of flavin reduction rate constants for syNOS, nNOS and CYPOR(n = 4). (B) Surface representation and model of $NADP^+$ (magenta) bound in the pocket of syNOS-Mon with loop 1050-1062 (orange-red and circled in black) in comparison to (C) nNOS bound to $NADP^+$ (grey) with corresponding loop 1002-1012 (aqua) circled Iin black. (D) Overlay of $NADP^+$ bound conformations of syNOS, nNOS and CYPOR W677X (1-676) (PDB: 1JA0) (green) over a consensus position of FNR-bound FAD (yellow). syNOS CTT residue 1440 blocks access of the nicotinamide ring to the isoalloxazine ring.

1180

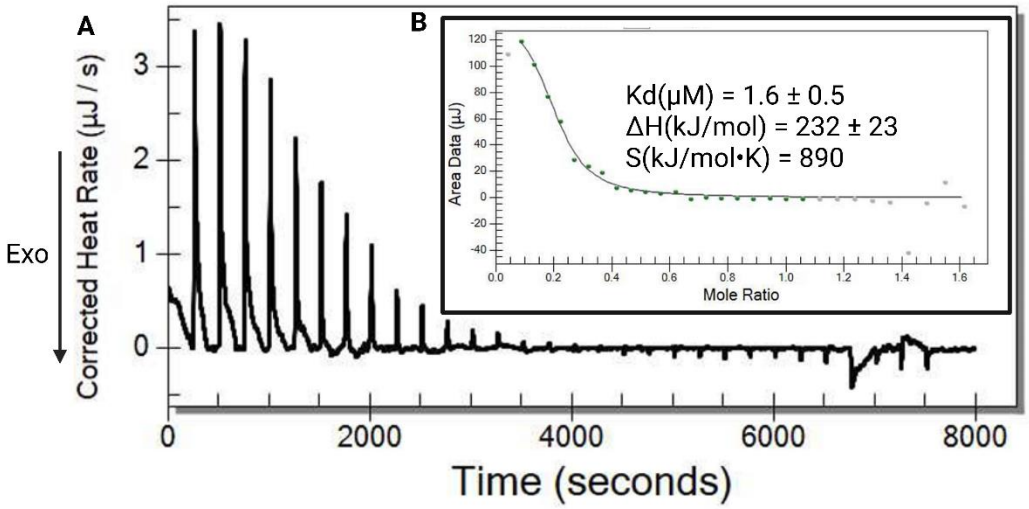

1181

1182 **Figure S17.** Isothermal calorimetric titration of Ca^{2+} with $syNOS_{C2}$ (residues 1-138). (A)

1183 Endothermic, baseline corrected isotherm of Ca^{2+} titrated into $syNOS_{C2}$. (B) Binding model fit

1184 with the accompanying thermodynamic parameters. (Samples were measured once)

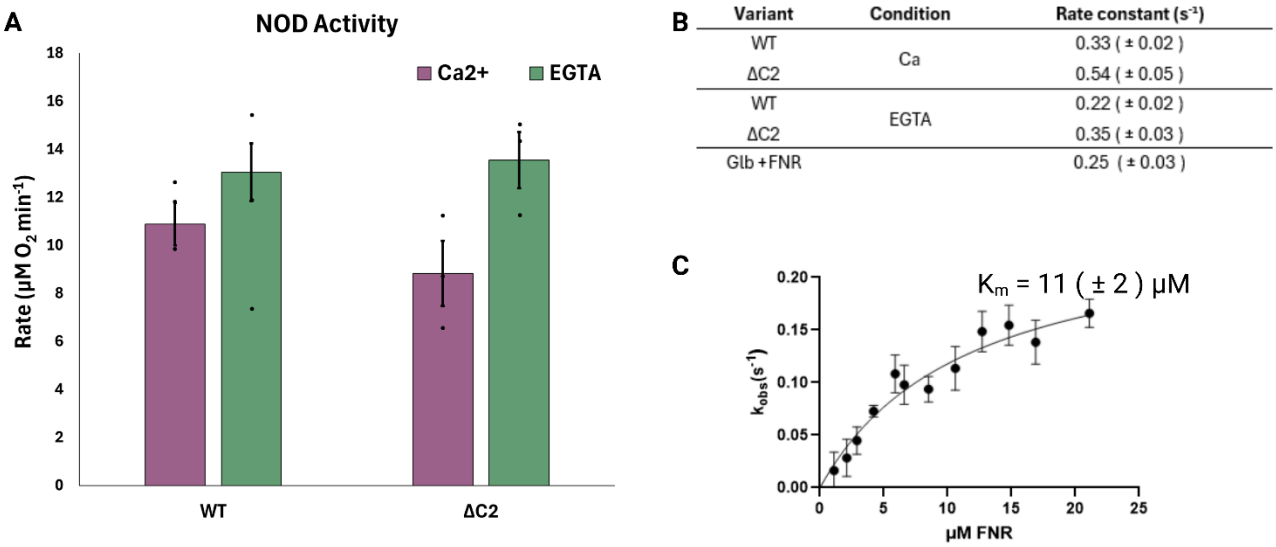

Variant	Condition	Rate constant (s^{-1})
WT	Ca	0.33 (± 0.02)
ΔC2		0.54 (± 0.05)
WT	EGTA	0.22 (± 0.02)
ΔC2		0.35 (± 0.03)
Glb +FNR		0.25 (± 0.03)

1185 **Figure S18.** SyNOS globin-based NOD activity and heme reduction rates. (A) NOD activity was

1186 measured by O2 consumption in the presence of the NO-donor NOC-7 and NADPH for WT and

1187 syNOS$_{\Delta C2}$ (n=3, except for syNOS$_{\Delta C2}$ + Ca^{2+} ; n = 2). (B) Heme reduction rate constants of
1188 syNOS$_{Glb}$ in the presence or absence of Ca^{2+} for WT or syNOS$_{\Delta C2}$ and the truncated
1189 syNOS$_{Glb}$/syNOS$_{FNR}$ couple in the absence of Ca^{2+}, with standard error represented. Statistical
1190 comparisons between groups were performed with a 2-way ANOVA with post hoc analysis using
1191 Tukey's multiple comparisons test, all comparisons were non-significant. (C) Michelis-Menten
1192 plot of truncated syNOS$_{Glb}$ reduced by varied concentrations of truncated syNOS$_{FNR}$ until
1193 saturation, with standard deviation represented. (Each data point reflects at least n = 3.)

1194

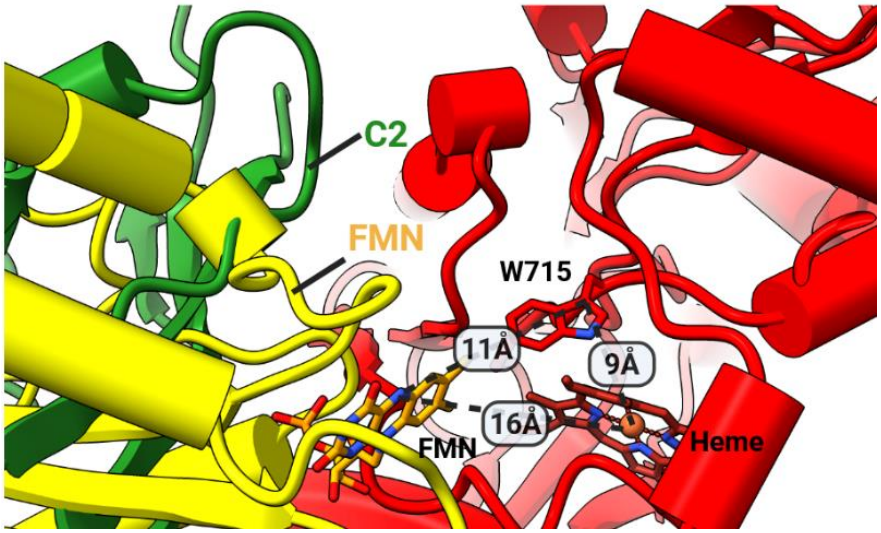

1195

1196 **Figure S19.** Output state predicted by AlphaFold3 with FMN-to-Trp715-to-Heme distances
1197 shown. Overlay of the C2 in the locked state (green) with the output Fld conformation (yellow)
1198 illustrates that the Fld is sterically blocked by the C2 domain in the NOS-Asym state. The AF3
1199 prediction was made with a minimal unit of two truncated syNOS chains: 1) residues 473-863
1200 (Oxy) and 2) residues 473-1003 (Oxy + Fld). Including additional domains did not predict
1201 interaction between syNOS$_{Fld}$ and syNOS$_{Oxy}$.

1202

1203

1204

1205

1206

1207

1208

1209

1210

1211

1212

1213

1214

1215